



**AFRL-AFOSR-VA-TR-2017-0071**

---

The Multiscale Interaction of Vibrational Energy Transfer and  
Turbulent Combustion in Supersonic Flows

**Phillip VARGHESE**  
**UNIVERSITY OF TEXAS AT AUSTIN**  
**101 EAST 27TH STREET STE 4308**  
**AUSTIN, TX 78712**

---

**04/04/2017**  
**Final Report**

Distribution A - Approved for Public Release

---

Air Force Research Laboratory  
AF Office Of Scientific Research (AFOSR)/RTA1  
Arlington, Virginia 22203  
Air Force Materiel Command

<b>REPORT DOCUMENTATION PAGE</b>		<i>Form Approved</i> OMB No. 0704-0188
<p>The public reporting burden for this collection of information is estimated to average 1 hour per response, including the time for reviewing instructions, searching existing data sources, gathering and maintaining the data needed, and completing and reviewing the collection of information. Send comments regarding this burden estimate or any other aspect of this collection of information, including suggestions for reducing the burden, to Department of Defense, Executive Services, Directorate (0704-0188). Respondents should be aware that notwithstanding any other provision of law, no person shall be subject to any penalty for failing to comply with a collection of information if it does not display a currently valid OMB control number.</p> <p><b>PLEASE DO NOT RETURN YOUR FORM TO THE ABOVE ORGANIZATION.</b></p>		
<b>1. REPORT DATE (DD-MM-YYYY)</b> 04-04-2017	<b>2. REPORT TYPE</b> Final Performance	<b>3. DATES COVERED (From - To)</b> 30 Sep 2012 to 29 Sep 2016
<b>4. TITLE AND SUBTITLE</b> The Multiscale Interaction of Vibrational Energy Transfer and Turbulent Combustion in Supersonic Flows	<b>5a. CONTRACT NUMBER</b>	
	<b>5b. GRANT NUMBER</b> FA9550-12-1-0460	
	<b>5c. PROGRAM ELEMENT NUMBER</b> 61102F	
<b>6. AUTHOR(S)</b> Phillip VARGHESE	<b>5d. PROJECT NUMBER</b>	
	<b>5e. TASK NUMBER</b>	
	<b>5f. WORK UNIT NUMBER</b>	
<b>7. PERFORMING ORGANIZATION NAME(S) AND ADDRESS(ES)</b> UNIVERSITY OF TEXAS AT AUSTIN 101 EAST 27TH STREET STE 4308 AUSTIN, TX 78712 US		<b>8. PERFORMING ORGANIZATION REPORT NUMBER</b>
<b>9. SPONSORING/MONITORING AGENCY NAME(S) AND ADDRESS(ES)</b> AF Office of Scientific Research 875 N. Randolph St. Room 3112 Arlington, VA 22203		<b>10. SPONSOR/MONITOR'S ACRONYM(S)</b> AFRL/AFOSR RTA1
		<b>11. SPONSOR/MONITOR'S REPORT NUMBER(S)</b> AFRL-AFOSR-VA-TR-2017-0071
<b>12. DISTRIBUTION/AVAILABILITY STATEMENT</b> : Distribution A - Approved for Public Release		
<b>13. SUPPLEMENTARY NOTES</b>		
<b>14. ABSTRACT</b> <p>The project was initiated to try and obtain answers to two basic questions:  (1) Do non-equilibrium energy distributions affect macroscopic reaction rates?  (2) Can these effects be leveraged for control in design of scramjets?</p> <p>The results obtained during the course of this project indicate that both these questions can be answered affirmatively, but the answers were surprising and non-intuitive. Our results have shown that in a co-flow hydrogen jet injector vibrational non-equilibrium delays ignition, but for a highly under-expanded hydrogen jet in a supersonic cross-flow (as in the Hyshot configuration) vibrational non-equilibrium results in a shorter ignition delay with the flame stabilizing further upstream. This demonstrates that vibrational nonequilibrium can be used to improve flame stability in a suitably designed scramjet.</p> <p>A high speed jet flame facility was designed and constructed. Rayleigh and Raman scattering measurements were made in this flow to obtain non-intrusive temperature measurements. Using a sheet of laser light single shot Rayleigh scattering was used to obtain instantaneous measurements of translational temperature in a plane. The Raman scattering measurements were point measurements and averaged over multiple laser shots to determine independent rotational and vibrational temperatures using high dispersion measurements of Stokes Raman scattering. The Rayleigh measurements were used to determine the probability distribution function (pdf) of the turbulent fluctuations.</p>		
<b>15. SUBJECT TERMS</b> nonequilibrium and aerothermodynamic, hypersonic and gas-surface interaction		

<b>16. SECURITY CLASSIFICATION OF:</b>			<b>17. LIMITATION OF ABSTRACT</b>  SAR	<b>18. NUMBER OF PAGES</b>	<b>19a. NAME OF RESPONSIBLE PERSON</b> LEYVA, IVETT
<b>a. REPORT</b>  Unclassified	<b>b. ABSTRACT</b>  Unclassified	<b>c. THIS PAGE</b>  Unclassified			<b>19b. TELEPHONE NUMBER</b> <i>(Include area code)</i> 703-696-8478

# The Multiscale Interaction of Vibrational Energy Transfer and Turbulent Combustion in Supersonic Flows

Philip Varghese, Noel Clemens  
The University of Texas at Austin

Venkat Raman  
The University of Michigan

**Grant No. FA9550-12-1-0460**

## Abstract

The project was initiated to try and obtain answers to two basic questions:

- (1) Do non-equilibrium energy distributions affect macroscopic reaction rates?
- (2) Can these effects be leveraged for control in design of scramjets?

The results obtained during the course of this project indicate that both these questions can be answered affirmatively, but the answers were surprising and non-intuitive. Our results have shown that in a co-flow hydrogen jet injector vibrational non-equilibrium delays ignition, but for a highly under-expanded hydrogen jet in a supersonic cross-flow (as in the Hyshot configuration) vibrational non-equilibrium results in a shorter ignition delay with the flame stabilizing further upstream. This demonstrates that vibrational non-equilibrium can be used to improve flame stability in a suitably designed scramjet.

A high speed jet flame facility was designed and constructed. Rayleigh and Raman scattering measurements were made in this flow to obtain non-intrusive temperature measurements. Using a sheet of laser light single shot Rayleigh scattering was used to obtain instantaneous measurements of translational temperature in a plane. The Raman scattering measurements were point measurements and averaged over multiple laser shots to determine independent rotational and vibrational temperatures using high dispersion measurements of Stokes Raman scattering. The Rayleigh measurements were used to determine the probability distribution function (pdf) of the turbulent fluctuations. Simulations of averaged Raman spectra of equilibrium flows using these pdfs were used to quantify the spectral distortion induced by averaging. The distortions were shown to be small provided one was not averaging at a point where the flame is only present intermittently. This facility was used to show that in the mixing layer of a non-reacting supersonic nitrogen jet in air, vibrational non-equilibrium of nitrogen in the mixing layer persists for a many jet diameters downstream of injection. Measurements were made in a high-speed jet flame and showed clear evidence of vibrational non-equilibrium upstream of the flame, and even in the jet core downstream of the flame base. Raman measurements on both nitrogen and oxygen gave rotational temperatures that were in excellent agreement with each other and with the translational temperature measured via Rayleigh scattering. The oxygen vibrational temperature was found to be in equilibrium with the rotational and translational temperature, but the nitrogen vibrational temperature was out of equilibrium. This result challenged the assumption of fast vibrational energy exchange between oxygen and nitrogen that was commonly used in simulations.

A highly scalable Quasi-Classical Trajectory (QCT) code was developed and tested using a published  $N_4$  potential. Non-equilibrium and equilibrium dissociation rates of  $N_2$  were calculated. The equilibrium rates were found to be in excellent agreement with calculations from another group using the same potential surface. The QCT code was used to determine non-equilibrium reaction rates for three critical reactions in the hydrogen combustion mechanism. The results of these calculations showed that the chain-branching combustion reactions, which are exchange reactions rather than dissociation reactions, are much less sensitive to vibrational temperature than is assumed in the standard Park two-temperature model. This key insight is critical to understanding why vibrational non-equilibrium leads to enhanced reaction rates in certain flow configurations. The relatively elevated translational temperature resulting from post-shock gases in the air-stream being vibrationally cold leads to a net increase in the reaction rates. The hydrogen fuel in the under-expanded injection jet is vibrationally “hot”, but this does not contribute significantly to the reaction since the vibrational temperatures are still low. The QCT code was also used to compute V-V exchange probability between nitrogen and oxygen at temperatures relevant to our laboratory experiments. The results confirmed the slow V-V exchange probability that produced the best match between simulations and experiments. These results are also relevant to scramjet inlet and isolator conditions. The QCT code will be made available to the community via a web repository.

Detailed numerical simulations were performed of the laboratory jet flame configuration and of a more realistic scramjet combustor configuration. The simulations of the laboratory flames showed that the experimental data could not be reproduced. A value at least 100 times smaller than the standard value of vibrational exchange probability between nitrogen and oxygen was found to give a better match to the experimental data. This value was then confirmed by QCT calculations of nitrogen-oxygen vibrational energy transfer rates over a wide range of temperatures. Detailed simulations of the Hyshot scramjet configuration using representative flight conditions showed that vibrational non-equilibrium enabled earlier ignition and thus a more stable flame than in a flow with complete equilibrium.

# **The Multiscale Interaction of Vibrational Energy Transfer and Turbulent Combustion in Supersonic Flows**

Philip Varghese, Noel Clemens  
The University of Texas at Austin

Venkat Raman  
The University of Michigan

**Grant No. FA9550-12-1-0460**

## **Introduction**

This report summarizes work completed under this grant in the areas of experiment, theory, and numerical flow simulations. In this final report we focus on the most recent results obtained under this grant.

## **1. Experimental effort**

We designed and constructed a high speed jet facility to enable experimental study of turbulent non-reacting jets and turbulent non-premixed flames. Laser based Rayleigh and high dispersion Raman scattering were used to probe the flow non-intrusively.

The facility has a small axisymmetric jet in a high temperature air coflow and is mostly constructed of stainless steel to prevent rust and allow for high temperature operation. The jet and coflow issue into open air, and the coflow velocity is less than 1 m/s. The jet gas is provided by compressed gas cylinders and the coflow air is provided by a blower pulling from the ambient room air. The coflow air is passed through a filter to remove the dust particles larger than 0.1  $\mu\text{m}$  in order to facilitate the flow diagnostics. The center jet flow issues through a CNC-machined stainless nozzle, which can be replaced to provide different flow velocities. Figure 1a shows the flow facility configuration for the air mixing studies, which consists of a Mach 1.5 round jet, with an 8 mm exit diameter, and centered in a 0.3 m diameter circular coflow chamber. For the reacting flow studies, a converging nozzle with 8 mm exit diameter was installed and a conical shroud reduced the coflow diameter to 100 mm. The reacting-flow configuration is illustrated below in Fig. 1b. This configuration enabled the collection lens used in Raman and Rayleigh scattering measurements to be brought closer to the probe laser beam increasing the light collection solid angle and thus improving signal-to-noise ratio (SNR).

This facility is similar to those used in previous jet-in-coflow studies<sup>1,2</sup> except that the coflow is electrically heated. The advantage of electrical heating is that it does not alter the chemical composition of the gases, while a vitiated coflow would include combustion products that could significantly affect the vibrational relaxation process. The coflow air is heated by a pair of 15 kW electric-resistance flow-through heaters. The maximum temperature of the heating element is rated at 1200 K. Two type K thermocouples inserted radially through the pipe wall 75 mm above the heating elements measure the temperature of the coflow in the settling chamber and allow feedback control of the heater power. The jet is similarly heated by a pair of 6 kW electric heaters. The coflow section is also fitted with a series of perforated plates, honeycomb and screens to provide flow conditioning. Translation of the entire assembly is provided by a stepper

motor and screw-driven translational stage for simple and precise (75  $\mu\text{m}$  accuracy) scanning of the flow.

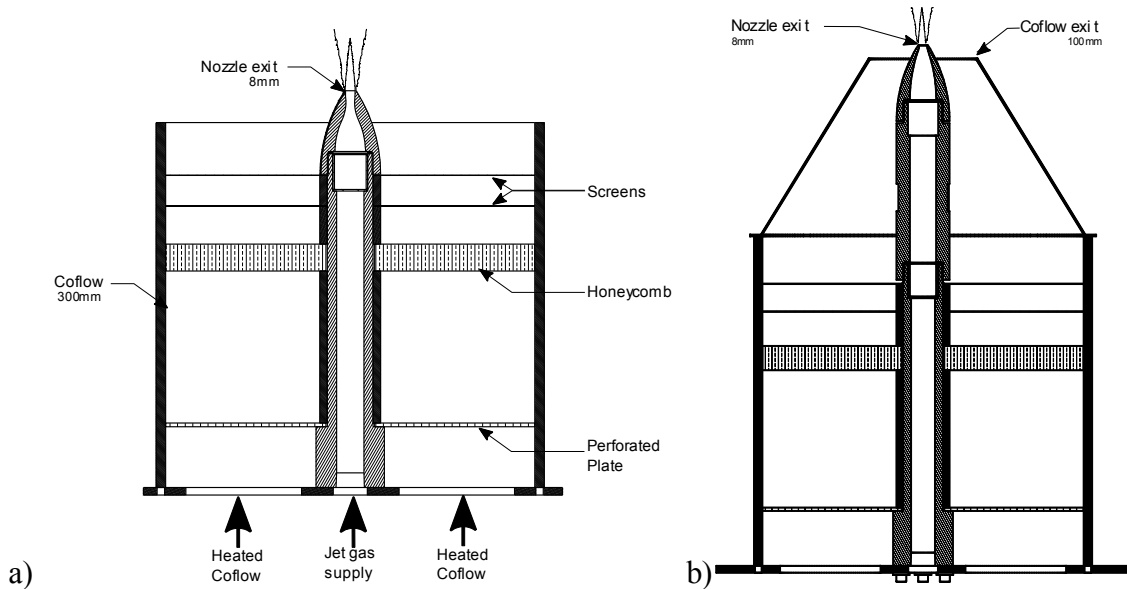


Figure 1: Cross-section view of the jet-in-coflow facility. (a) Air-Air mixing configuration with Mach 1.5 nozzle installed, and (b) reacting-flow configuration with converging nozzle and coflow shroud.

### Air-Air mixing experiments

In one set of experiments, vibrational non-equilibrium was studied in the shear layer that developed between a supersonic air jet and the co-flow of heated air. The operating conditions are summarized in Table 1. The air jet was operated in a perfectly expanded state where the exit pressure was matched to the ambient pressure of the room. The Raman scattering measurements were made in the axisymmetric shear layer located 12 mm downstream of the jet exit. The shear layer thickness,  $\delta$ , shown in the table is defined by the 5-95% width of the mean temperature profile (determined by Rayleigh scattering). The characteristic timescale of the mixing in the shear layer, which will be used to compare with the relaxation time of the vibrational energy, was defined as the eddy turnover time,  $\delta/\Delta U$ , where  $\Delta U$  is the difference between the speed of the jet and the coflow. This timescale is very short relative to the vibrational relaxation times for  $\text{N}_2$  shown below, and therefore a non-equilibrium condition is expected.

Table 1: Operating conditions and relevant flow parameters

Jet	Coflow	$T_{jet}$	$T_{coflow}$	$M_{jet}$	$s = \frac{\rho_{coflow}}{\rho_{jet}}$	$M_c$	$\delta (z=12 \text{ mm})$	$\tau_{mix} = \frac{\delta}{\Delta U}$
Air	Air	210 K	850 K	1.5	0.25	0.51	2.3 mm	5 $\mu\text{s}$

### Spontaneous Raman scattering setup

Figure 2 shows the schematic of the set up used for Raman spectroscopy. The excitation energy for the light scattering is provided by a frequency doubled, diode pumped Nd:YAG laser (Coherent Corona) with pulse energy of 4 mJ at 532 nm and operated at 10 kHz repetition rate. The pulse duration is  $\sim 160$  ns,  $M^2$  is 25, the beam width is 5 mm and the beam divergence is 5

mrad. The laser light is switched between the alignment mode and the experimental modes using the combination of a polarization rotator and a polarizing beam splitter. In the experimental mode, the beam splitter is removed from the set up and the polarization rotator is adjusted to maximize the Raman signal in the direction of the collection optics. The laser beam is focused using a 40 cm focal length lens. The scattered light is collected by a Nikon 105 mm f/2.8 camera lens and focused into the entrance aperture of a HoloSpec f/1.8 spectrograph manufactured by Kaiser Optical Systems, Inc. The front surface of the collection lens is positioned about 22 cm from the nozzle centerline. The camera lens used is corrected for chromatic aberrations. The elastically scattered light is filtered out by a SuperNotch filter with O.D. > 4.0 and bandwidth <  $350 \text{ cm}^{-1}$ . Light is dispersed by the HDG-608 transmission grating, which has an average dispersion of  $\sim 0.03 \text{ nm}$  per pixel. Both the notch filter and the grating are available from Kaiser Optical Systems, Inc. The signal is recorded using an ICCD camera with an 18 mm wide HBF Gen III intensifier. The intensifier's quantum efficiency is 44% at 607 nm, which is near the peak of the  $Q$  branch of the Stokes signal from  $^{14}\text{N}_2$ . The CCD array has  $1024 \times 256$  pixels and each pixel has dimensions of  $26 \mu\text{m} \times 26 \mu\text{m}$ . The spectral coverage is 595 to 620 nm, the slit width of the spectrograph is  $100 \mu\text{m}$  and the magnification of the combined collection and dispersion optics is approximately 0.8. The exposure time of the sensor was 20 s, i.e., each data set is obtained from the equivalent of 800 J of incident energy. Such high incident energy is necessary to obtain good signal to noise ratio (SNR) in the low-intensity spectrally resolved  $O$  and  $S$  branches. As shown in Fig. 3, the intensity of the  $O$  and the  $S$  branches are 2-3 orders of magnitude less than that of the  $Q$  branch. This large dynamic range is made possible by the large vertical sensor area on which the signal is collected.

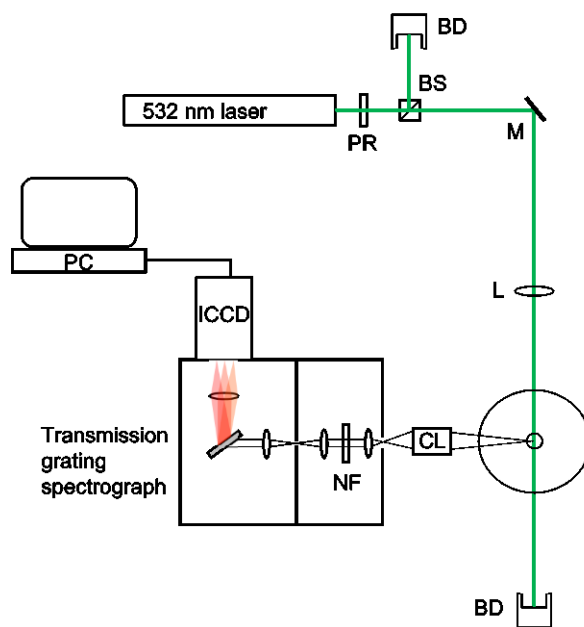


Figure 2: Schematic of the Raman set up; BD, beam dump; BS, beam splitter; PR, polarization rotator; M, mirror; L, lens; CL, camera lens; and NF, notch filter.

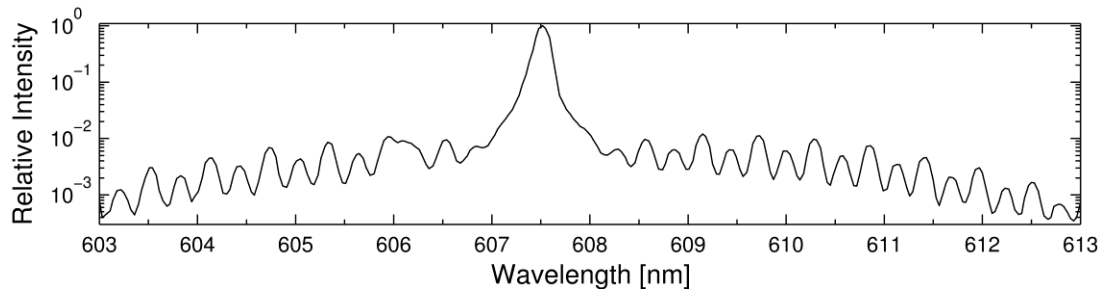


Figure 3: Sample Raman spectrum from  $N_2$  in the jet at 210 K. Note logarithmic vertical scale.

The spectral calibration procedure is as follows. The raw data is measured in terms of counts as a function of the pixel positions along the dispersion axis of the CCD array. The wavelength calibration converts pixels to wavelength, and the intensity calibration converts counts to intensity. The wavelength calibration is performed by comparing the pixel positions of the emission lines from a neon calibration lamp with their respective positions tabulated in the NIST database. The pixel positions of the individual neon lines are obtained to sub pixel resolution by curve fitting the instrument line shape model to the recorded spectrum. The instrument line shape function is modeled by convolving a trapezoid function and a Lorentzian. The free parameters of the line shape function are the half base width and the half top width of the trapezoid, and the Lorentz width. The intensity calibration factors are obtained by taking the ratio of the Planck's function at 1000 K to the counts recorded from a blackbody source (CI Systems SR-20) at the same temperature. Additional details on the data calibration procedure are described in Utsav, et al.<sup>3</sup>

### Thermometric Rayleigh imaging setup

Planar laser Rayleigh imaging was used to provide an instantaneous measurement of the gas temperature. The light source for the 2D Rayleigh scattering is a 532 nm frequency-doubled Nd:YAG laser (Spectra-Physics GCR-150) operated at 10 Hz. The pulse width was 10 ns and the pulse energy was 300 mJ. The beam was first expanded using a pair of cylindrical lenses (with focal lengths -40 mm and 130 mm, respectively), and then focused with a 500 mm focal length positive cylindrical lens. The resulting laser sheet thickness was measured by traversing a knife-edge through the beam while monitoring the power; the resulting sheet thickness was 130  $\mu\text{m}$  (FWHM). The sheet height was  $10 \pm 1$  mm.

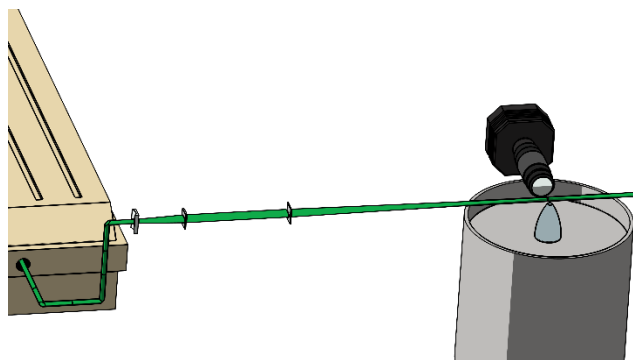


Figure 4: Schematic diagram of the Rayleigh scattering setup.

The Rayleigh scattering was imaged using a back-illuminated CCD camera (PixelVision SV512V1). A pair of Nikon 50mm f/1.4 lenses were used in a “front-to-front” configuration and operated at infinite conjugate ratio and unity magnification. The imaging field of view was 12 mm × 12 mm. Resolution of the imaging system was characterized by measuring the step response function by the scanning knife-edge method.<sup>4</sup> A knife-edge was traversed through the object plane as images are recorded from a uniform light source. By plotting the response in a single pixel as a function of knife-edge position, the line spread function was obtained. Fitting an error function to the response curve showed the full width at half maximum to be 29 μm. The resulting short working distance of the lens configuration required that the lenses be located within the hot coflowing air. A lens protection and cooling system (not pictured in Figure 4) kept the hot co-flow gas from damaging the lenses and camera. Alteration of the shear layer by this intrusion is minimal due to the high velocity ratio between the jet and coflow.

A set of sample Rayleigh scattering images is shown in Fig. 5. The physical region being depicted here is approximately 5 mm × 6 mm in the radial and streamwise directions, respectively, and it is centered 12 mm downstream of the nozzle exit. The denser cold jet is on the left while the hot coflow is on the right. The shear layer exhibits many small fingers of cold jet fluid reaching into the hot flow without the coherent “roller” structures. This behavior is consistent with previous study of compressible mixing layer structure.<sup>5,6</sup>

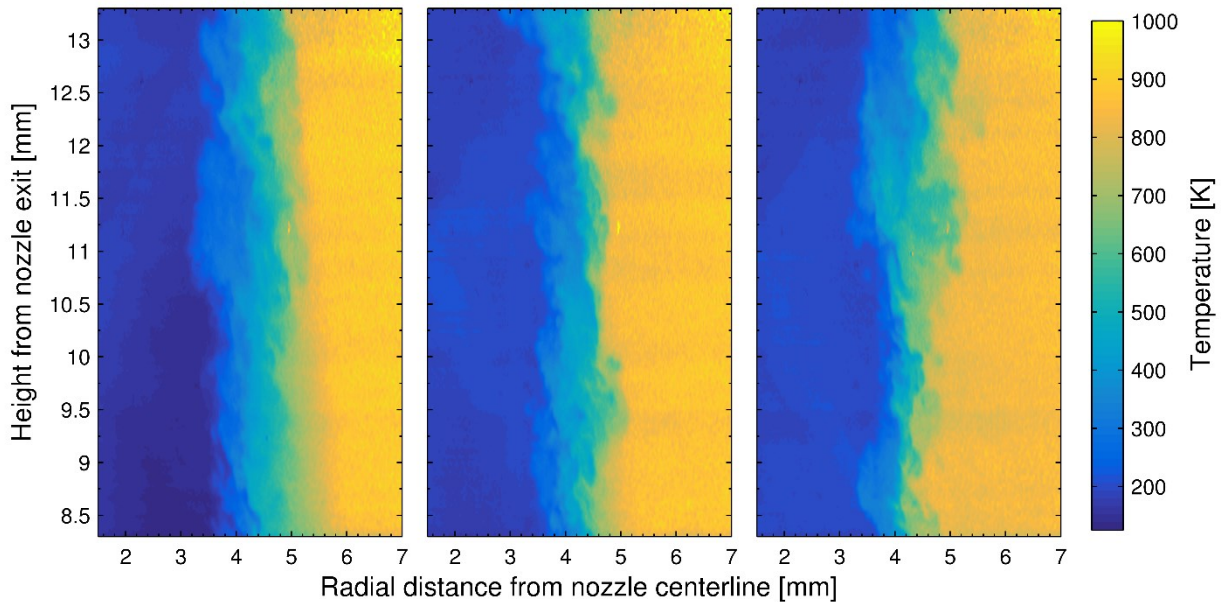


Figure 5: Sample Rayleigh scattering images

### *Rayleigh and Raman Temperature Measurements*

Figure 6 shows temperature profiles 12 mm downstream of the nozzle exit obtained using the previously described techniques. The radial coordinate is non-dimensionalized in a manner consistent with previous high-speed mixing studies:  $\eta \equiv \frac{r-r_{0.5}}{\delta}$ , where  $r_{0.5}$  is the radial location of the mean temperature of the two freestreams. The Rayleigh-based profile is the average temperature field computed from the 77 images captured during the 3 minute run. The thermocouple measurements were obtained using 2 thermocouples with different bead diameters.

The results are then extrapolated to an infinitesimally small bead size to account for the error due to bead radiation. Temperatures from the Raman scattering measurements are shown at the discrete locations which were probed. Vibrational temperatures are omitted where the air temperature is too low ( $<450$  K) for a meaningful fit, which occurs when the hot-band intensity recedes into the measurement noise. The error bars in Fig. 8 for the Raman temperature measurements were determined as follows. Residuals between the collected spectra and the fit results were stored in a library. These residuals are added to a simulated spectrum at known temperature and then fit for temperature. The best fit value of temperature from the spectral fit to the noisy simulated spectrum is then used to estimate the uncertainty in temperature caused by noise in the data and temperature variations in the probe volume during the collection time.

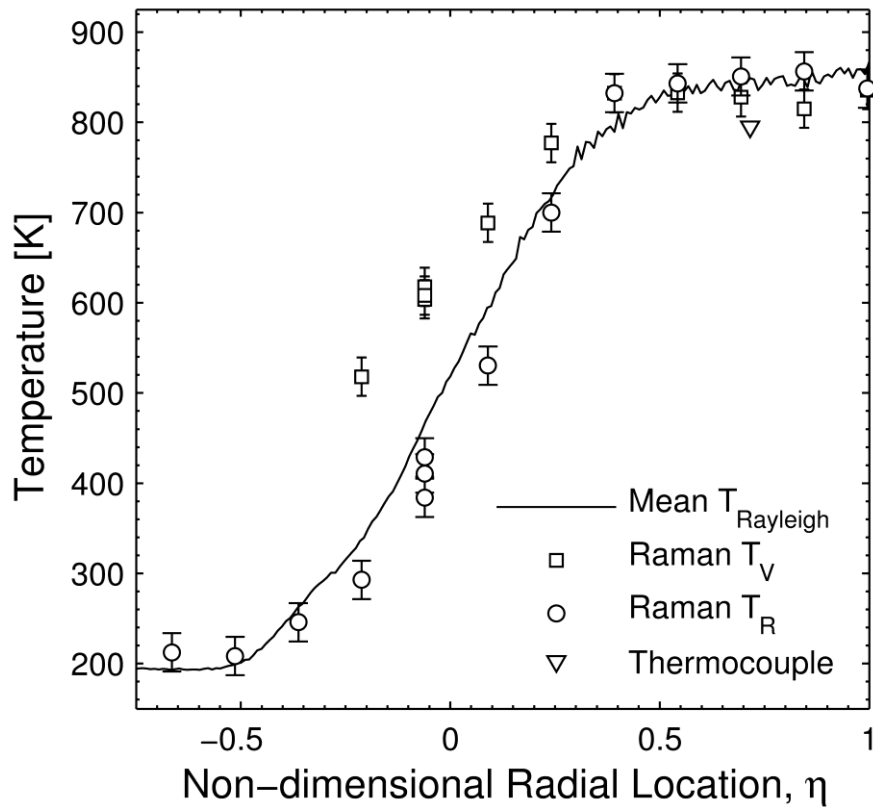


Figure 6: Various temperature measurements as a function of radial location at 12 mm downstream of the nozzle exit.

As shown in Fig. 6, there is good agreement between the Raman, Rayleigh and thermocouple temperature measurements outside the shear layer. There is also minimal difference between  $T_V$  and  $T_R$  away from the shear layer, which is expected for flow that is in equilibrium. On the hot side of the shear layer, the effect of slow vibrational relaxation is clearly evident. The vibrational temperature within the shear layer remains higher than the flow temperature as the energy relaxes more slowly from the initial inflow step function profile. This can be imagined as the vibrational energy “lagging” behind the rapid cooling of the flow by remaining nearer to the freestream temperature. The rotational temperature inferred from the Raman scattering measurements agrees with the Rayleigh-derived temperature to within 50 K at all locations. One should note that the Raman rotational temperature measurements are consistently lower than the

Rayleigh scattering results in the shear layer. This may not be an error, but instead could be a result of the space and time averaging process. Because higher density fluid scatters light more effectively, the collected Raman spectra will be weighted toward the colder side of the temperature probability density function (PDF) within the measurement volume. The effect of this spatiotemporal averaging is evaluated further in the following section.

#### *Distinction between Compound and Non-equilibrium Spectra*

One drawback of using time-averaged Raman spectroscopy in a turbulent flow is the possibility of inferring false levels of non-equilibrium owing to the effect of averaging on the spectra. In particular, since the Raman spectral intensities are a non-linear function of temperature, then the average spectrum in a flow with fluctuating temperature, is not the same as the spectrum associated with the average temperature. It is critical that the magnitude of this effect is determined before conclusions can be drawn regarding the degree of non-equilibrium. Our approach is to create a compound spectrum, which is the average of equilibrium spectra at different temperatures, and then to fit the compound spectrum to obtain estimates of rotational and vibrational temperature. If the non-linear weighting effect is negligible then the fitting process will show no non-equilibrium in the compound spectrum.

The compound equilibrium spectrum is simulated by adding the spectra computed at temperatures corresponding to the actual temperature fluctuations in the shear layer as measured by Rayleigh scattering. The Rayleigh temperature measurements, with higher spatial and temporal resolution, provide information on both the spatial and temporal temperature distributions within a given Raman probe volume. As stated previously, the Rayleigh scattering measurements have a spatial resolution of 29  $\mu\text{m}$  in the imaging plane and an exposure equal to one laser pulse width, 10 ns. Conversely, the Raman spectra are recorded from a  $1.1 \times 0.33$  mm region and integrated over 20 s. The probability density functions of temperature for several of the Raman sampling locations are shown in Fig. 7. These sampling regions simulate the physical region from which spectra are collected by the spectrograph. Equilibrium Raman spectra are calculated at each of the temperatures shown in the PDF in Fig. 7 and are averaged to generate a compound spectrum at each location. In order to make the simulated spectrum more similar to the experimental data, the residuals from a curve fit to the Raman data are added to the simulated compound spectrum. The non-equilibrium Raman code is then used to fit the simulated noisy compound spectrum. We find that the non-linear weighting does indeed cause some apparent non-equilibrium since  $T_R$  and  $T_V$  differ; however, this effect is less than 50 K at all locations. This difference is significantly less than the difference between these values obtained from the experimental data shown in Fig. 6, which indicates clearly that the recorded spectrum is not just the superposition of equilibrium Raman spectra.

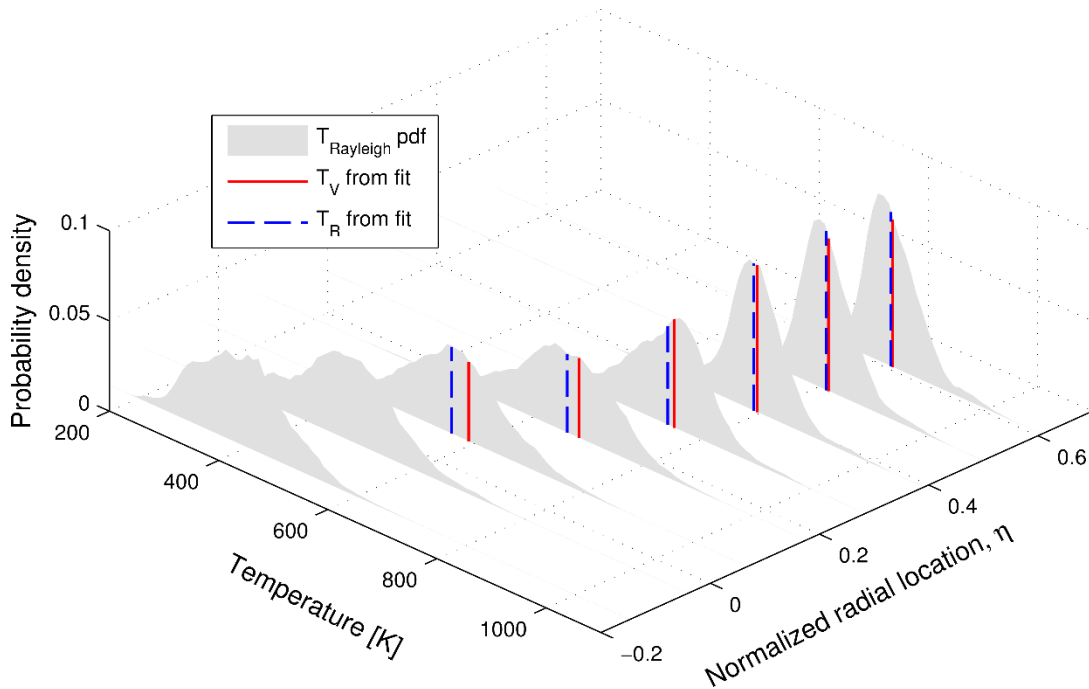


Figure 7: Rayleigh temperature PDFs at various Raman probe regions with the temperatures obtained from spectral fitting the average Raman spectra over the PDF.

It is worth noting that the compressible nature of the mixing layer and subsequent suppression of large-scale “roller” structures may help to reduce the temperature fluctuations in the shear layer and hence the magnitude of the non-linear weighting error. The narrowing of local PDFs with increasing compressibility has been found in both planar<sup>7,8,9</sup> and axisymmetric mixing layers.<sup>10</sup> In other flows where the fluctuations may be higher, the local PDF for each measurement may be broad enough that the difference between  $T_V$  and  $T_R$  in a compound spectrum may be of the same order as the fitting results from the actual Raman scattering data. Because of this, the local temperature fluctuations must be quantified when extending this technique to other flow environments.

#### *Effect of CO<sub>2</sub> Addition*

Figure 8 shows the result of several spectra rapidly collected at one location near the center of the shear layer. Samples were taken first with the air-air mixing case presented above and then CO<sub>2</sub> was seeded into both streams at a mole fraction of approximately 5 and 10%. The suppression of the hot band at 606.5 nm, as a result of the addition of CO<sub>2</sub>, signifies the reduction in the  $v = 1$  population. Spectral fits showed that the difference between  $T_V$  and  $T_R$  decreased from 135 K, without any addition of CO<sub>2</sub>, to 90 K with the addition of 10 % CO<sub>2</sub>. This reduction in non-equilibrium confirms that the presence of CO<sub>2</sub> accelerated the  $V$ - $T$  relaxation of N<sub>2</sub> as expected, while also reinforcing the fact that true  $V$ - $T$  non-equilibrium is being measured in this flow.

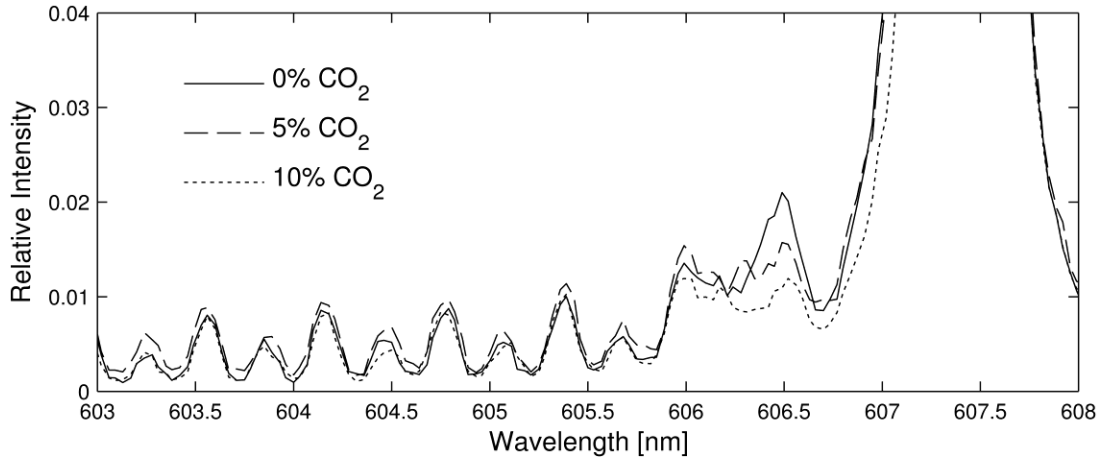


Figure 8: Effect of CO<sub>2</sub> addition on vibrational hot band population

### *Competing Excitation and De-excitation Processes*

Thermal energy transfer between the two streams occurs as hot and cold packets of fluid in local vibrational-translational equilibrium are entrained from the low and high speed sides of the layer, respectively. If one assumes this process to have equal forward and reverse relaxation rates, the temperature profiles would be expected to evolve in a manner similar to a one-dimensional diffusion process. In this scenario, since density effects have been ignored, the process appears to behave in a symmetrical fashion. This would be analogous to a shear layer in which the mass entrainment from both sides of the layer is equal so that the mean temperature inside the layer would match the mean of the two freestreams. The entrainment ratio of the shear layer can be predicted by the relation given by Dimotakis.<sup>11</sup> Because the velocity ratio ( $r$ ) in our flow is very low, the relation simplifies to

$$E_m(r \rightarrow 0) = 1.68/s^{1/2},$$

where  $s$  is the density ratio across the shear layer. We estimate the mass entrainment ratio,  $E_m$ , for the air-air mixing case to be approximately 3.3, which indicates a strong bias in mass flux entering the shear layer from the high-speed (cold) side. This entrainment asymmetry will reduce the mean temperature of the shear layer so that the hot side will now be much further from the equilibrium temperature. This effect is illustrated in the cartoon profiles in Fig. 9, which illustrate how the apparent non-equilibrium would appear larger in magnitude for the cooling process for entrainment ratios greater than one, which agrees with the temperature profiles presented above.

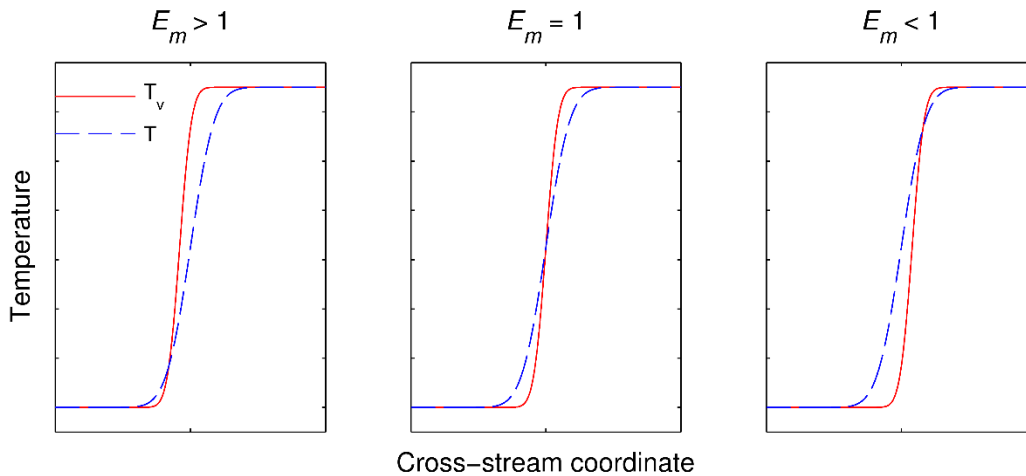


Figure 9: Theoretical depiction of effect non-unity entrainment ratio has on temperature profiles.

Within each probe volume, there is a local averaging effect as fluid packets that originate on either side of the layer are present. This averaging effect can reduce the apparent magnitude of non-equilibrium as molecules with excess vibrational energy and those with a vibrational deficit will both be present and mixed at a molecular level. To isolate this effect, dissimilar species can be used in order to track molecules from each side of the layer. Because the jet temperature is too low to probe with the current technique, it is convenient to continue to use air on the hot side of the layer and introduce the Raman inactive species, argon, in the jet. This allows the tracking of vibrationally hot  $N_2$  molecules as they are entrained and mixed with the cold jet.

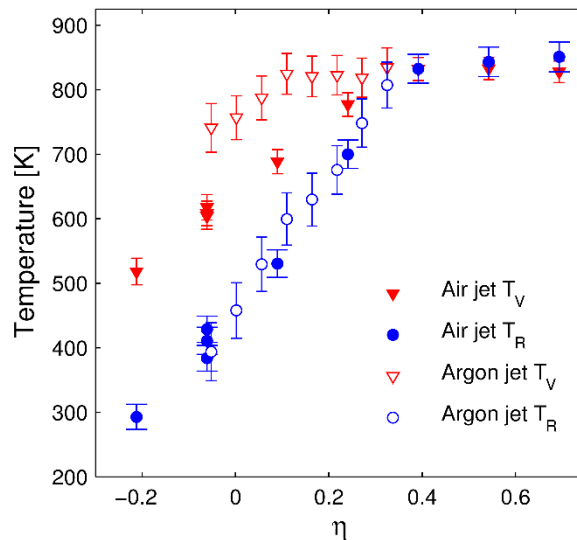


Figure 10: Temperature profiles for the air-air mixing and argon-air mixing cases.

In Fig. 10, the results are presented for an argon-air case and compared with the air-air case shown in Fig. 6. The freestream conditions are also presented in Table 2. The conditions for the argon-jet case are different from that of the air-jet case since the ratio of specific heats is different and so the nozzle must be run off-design to achieve pressure matched conditions at the

exit. The profile is truncated where the local concentration of nitrogen is too low for the fitting code to converge to a meaningful result.

Table 2: Experimental conditions during the air-air and argon-air mixing cases

	Air-Air	Argon-Air
$T_{jet}$	210 K	170 K
$T_{coflow}$	850 K	850 K
$M_{jet}$	1.50	1.55
$\gamma_{jet}$	1.4	1.67
$Re_d$	$8 \times 10^5$	$6.3 \times 10^5$

The non-equilibrium can be observed deeper into the layer when vibrationally active molecules only originate on the hot side of the layer. This confirms that the hot-to-cold relaxation process actually produces a stronger non-equilibrium than is suggested by Fig. 6. Therefore, a converse process of vibrationally cold molecules relaxing to a higher temperature must also exist in the layer. Because this is an effect that is present at the molecular level, and the molecules are distributed homogeneously within the probe volume, one cannot resolve this by improving the spatial resolution of the measurement. In a shear layer with identical species on each side, the only true way to separate the two processes would be to track on which side of the layer each molecule originated from. Because this is not possible in a real flow, this averaging effect will be present in any measurement made in a layer with vibrationally active species in both freestreams.

### Summary of jet mixing studies

The effect of slow vibrational relaxation in a high-speed shear layer was measured using a combination of time averaged spontaneous Raman scattering and instantaneous planar Rayleigh scattering. The spectral fitting Raman procedure is sufficient to detect non-equilibrium when the local temperature is above 450 K. It was only possible to measure the non-equilibrium between the vibrational and the rotational energy. It was not possible to identify non-equilibrium vibrational distributions because only the fundamental and the first hot bands were significantly populated. The introduction of CO<sub>2</sub>, a quenching species, suppressed the hot band as expected, and thus provided validation that the non-equilibrium observed in the air-air case is physical rather than an artifact of the measurement technique. The overall shape of the vibrational and rotational temperature profiles was shown to be a result of two competing non-equilibrium processes occurring within the shear layer. This averaging effect, which occurs on a molecular level, will be present in any shear-layer-induced non-equilibrium process that has the same vibrationally participating species on both sides of the layer.

### High-speed jet flame experiments

In the following study, the same techniques were applied to high-speed jets of combustible gas mixing with hot air coflow. Several flame conditions were run, which are summarized in Table 3 below. For each run, the coflow temperature was kept at 1000 K. The jet velocity values in Table 3 are calculated based on input mass flow rates and thermocouple measurements. The flow conditions in this study were chosen such that the flame stabilized at approximately the same

liftoff height from the nozzle exit. Each condition provides a flame that auto-ignited immediately at the onset of fuel flow. The first two fuel mixtures listed consist of  $H_2$  with diluents  $N_2$  and Ar to simplify the non-equilibrium relaxation mechanism to a system of diatomic and atomic species, minimizing the computational expense of modeling these cases in companion CFD simulations. The  $H_2/N_2$  and  $H_2/Ar$  cases also provide a comparison pair with and without the presence of vibrationally cold  $N_2$  from the jet. The  $H_2/CH_4$  fuel mixture is the same as in [69] and provides a Rayleigh cross section which is identical to that of air. This cross section matching allows for the application of Rayleigh thermometry to quantify the effect of temporal averaging in the Raman measurements in a similar fashion to the air-air mixing study. Figure 11 below shows the average lifted flame location for the  $H_2/N_2$  flame case as marked by a long exposure  $OH^*$  chemiluminescence image. The flame lifts approximately 5 diameters from the nozzle exit in this case and is highly turbulent. Owing to the much higher speed of sound for the combustible mixtures, all the cases for this study were subsonic. For all cases the stoichiometric mixture fraction,  $Z_{stoich}$ , is relatively small and so the flame resides mainly on the low-speed side of the shear layer.

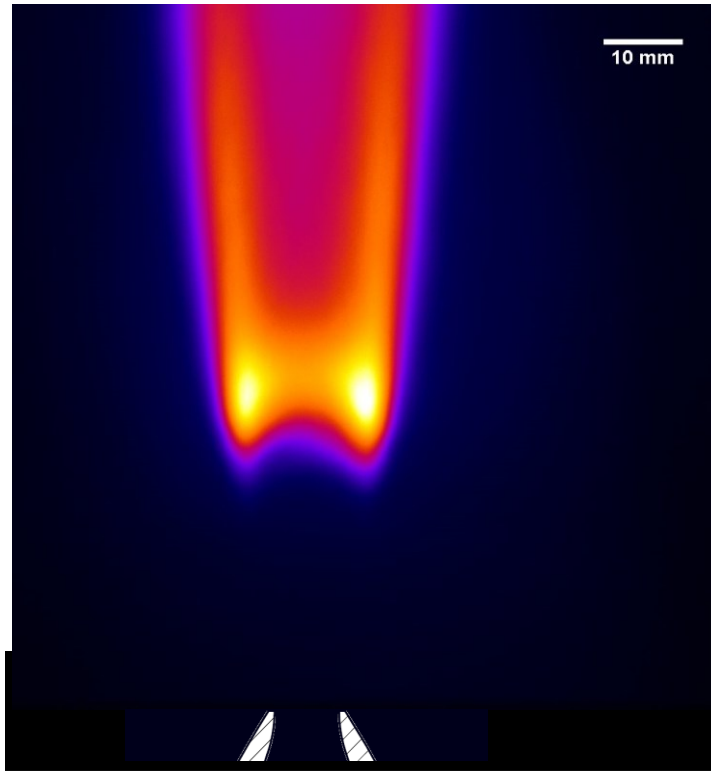


Figure 11: Time-average image (false color) of  $OH^*$  chemiluminescence for the  $H_2/N_2$  flame case

Table 3: Summary of run conditions

Case	Jet (by mol.)	Coflow	$U_{jet}$ [m/s]	$Re_d$	$T_{o,jet}$ [K]	$Z_{stoich}$
$H_2/N_2$	68% $H_2$ , 32% $N_2$	Air	540	75,100	560	0.181
$H_2/Ar$	75% $H_2$ , 25% Ar	Air	505	77,000	570	0.183
$H_2/CH_4$	62% $H_2$ , 38% $CH_4$	Air	300	27,400	550	0.048

For this study, several changes were made to the Raman and Rayleigh scattering measurements. The laser used was a frequency doubled diode-pumped Nd:YLF laser (Coherent Evolution 90) operated at 5 kHz repetition rate and an average power of 60W. The 105mm f/2.8 camera lens was no longer used for the collection optics. Instead, a pair of f/2.2 150 mm diameter achromatic lenses (Special Optics 54-120-260) operated at infinite conjugate ratio was used. The smaller f-number enabled reduced integration times to achieve the same signal levels as with the previous collection optics. For this study, we also obtained a grating which allowed for the measurement of O<sub>2</sub> Stokes Raman scattering by giving spectral coverage of 562 to 583 nm. Owing to the heat generated by the flame, the paired lens setup was not used for the Rayleigh scattering measurements obtained in this study. Instead a forward-facing Nikon 50mm f/1.2 lens was used with 20 mm of extension to obtain sufficient magnification while maintaining a large enough working distance to protect the lens and camera from thermal damage. The incident light for the Rayleigh scattering was provided by frequency-doubled Nd:YAG laser delivering 1J per pulse at a 10 Hz repetition rate. The scattered light was imaged by a CCD camera (PCO 1400) with 2×2 pixel binning to increase the signal-to-noise ratio. The field of view for this setup was approximately 17 mm and 10 mm in the radial and axial directions respectively.

### **Confirmation of non-equilibrium in measured spectra**

In the air-air mixing study, the Raman-based measurements of non-equilibrium were aided by the use of Rayleigh thermometry that was enabled by the constant Rayleigh cross-section of the air-air system. The same analysis can be applied to the current H<sub>2</sub>/CH<sub>4</sub> Rayleigh thermometry results to confirm that temperature fluctuations within the probe volume do not lead to excessive false non-equilibrium. Temperature values for regions of the flow field of the same physical dimension as the Raman measurement were extracted from a set of 1000 Rayleigh images. The probability density function within each of these regions is shown in Fig. 12. Equilibrium Raman spectra are calculated and summed to simulate the spatial and temporal averaging that occurs during a Raman measurement. The resultant composite spectra are then fitted for vibrational and rotational temperatures, which are also presented for each location in Fig. 12. This modeling exercise shows that the actual temperature fluctuations cause a maximum discrepancy between  $T_v$  and  $T_R$  of at most 15 K, which is significantly less than the magnitude of non-equilibrium seen in the collected spectra; however, this is not expected to be the case in a region over which the flame is only present intermittently. Figure 13 shows sample Rayleigh thermometry images from the H<sub>2</sub>/CH<sub>4</sub> flame, which illustrate the highly intermittent nature of the flame. The flame liftoff height fluctuates over a distance that is larger than the imaging field of view. A time-averaged Raman measurement made in this region would be integrating over gas temperature variations of over 1000 K and could not be used reliably to detect vibrational non-equilibrium.

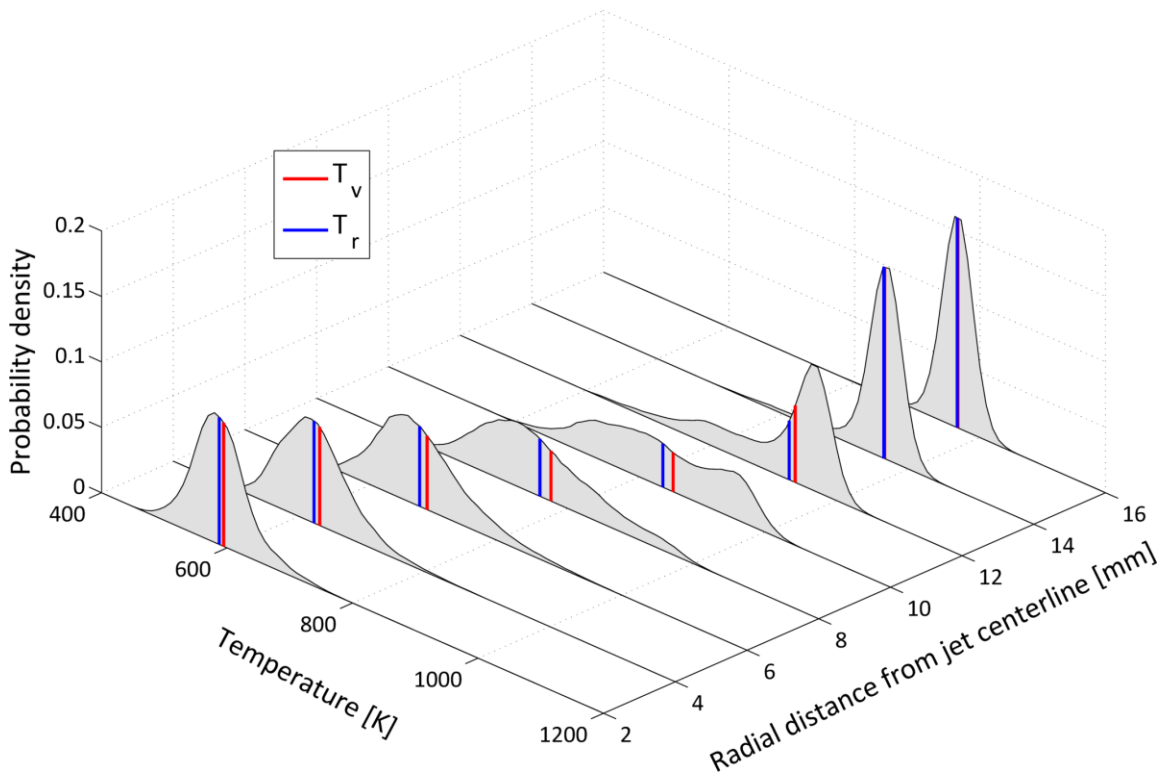


Figure 12: Temperature probability density functions extracted from Rayleigh thermometry images along with temperatures obtained by applying the fitting code to similarly distributed equilibrium spectra. The profile shown is 6 diameters downstream of nozzle exit.

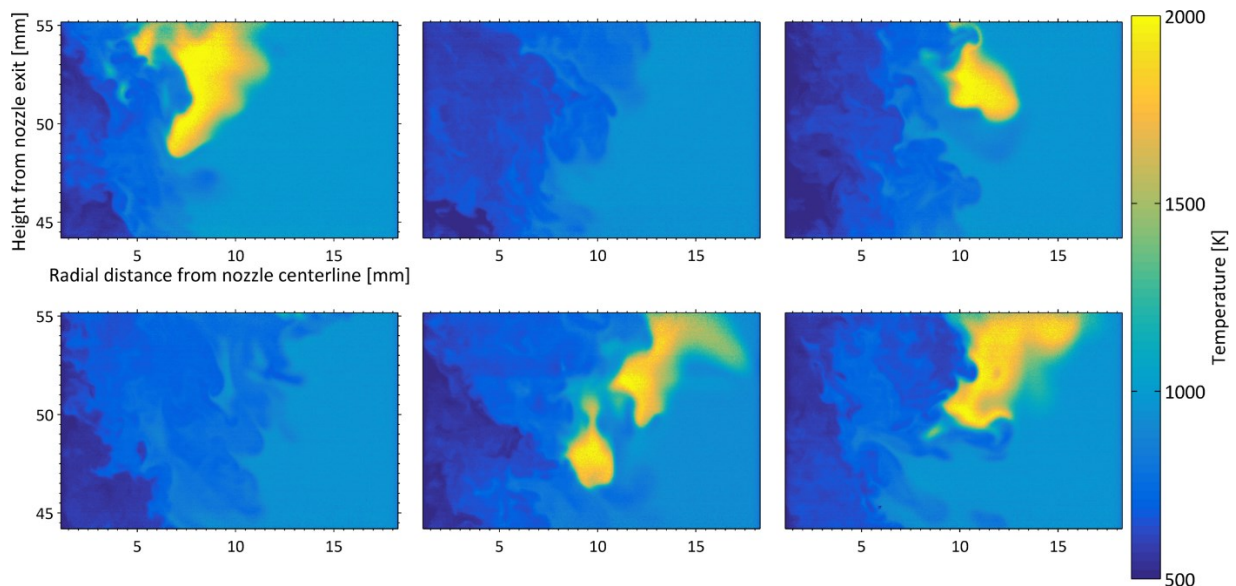


Figure 13: Sample uncorrelated Rayleigh thermometry images for  $H_2/CH_4$  flame.

### Raman measurements in hydrogen flames

Using hydrogen as fuel simplifies the combustion chemistry and allows for simpler models to be used for CFD validation. The lack of carbon-containing polyatomic species also significantly

simplifies the modeling of V-V and V-T energy transfer. Radial shear layer profiles were taken at various downstream locations (Fig. 14) to characterize the non-equilibrium in the shear layer upstream of the flame.

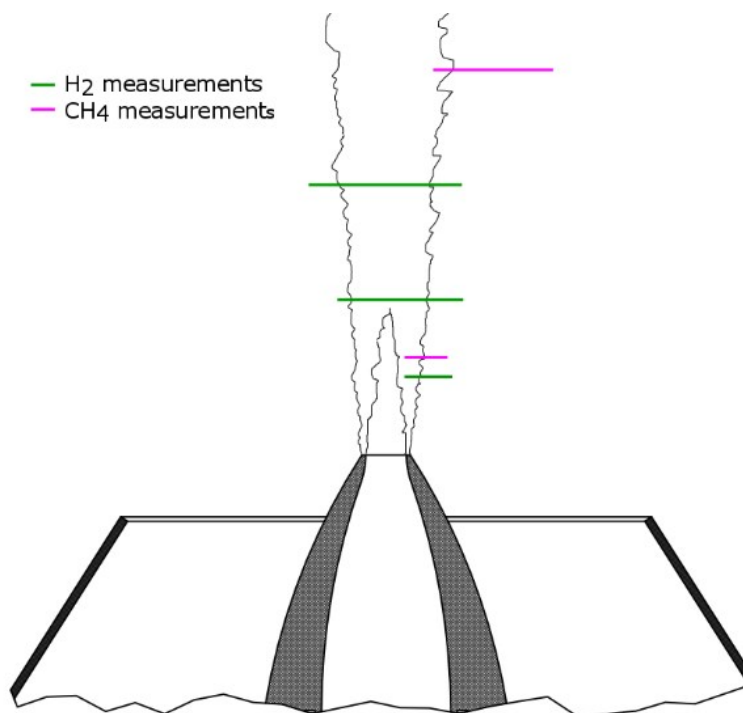


Figure 14: Schematic diagram of the Raman scattering measurement locations (to scale).

Figure 15a shows vibrational and rotational temperature measurements at a location that is in the non-reacting mixing region upstream of the lowest extent of the unsteady flame base. The rotational temperatures of  $N_2$  and  $O_2$  agree very well, because R-T relaxation is very fast. This consistency between measurements, which were performed with separate runs and using a different spectral region, provides verification of the measurement accuracy. From the vibrational temperature measurements in Fig. 15a it is apparent that the  $N_2$  is out of thermal equilibrium within the shear layer, as seen in our previous measurements,<sup>12</sup> but interestingly the  $O_2$  seems to be in complete equilibrium throughout the mixing region. This difference among  $N_2$  and  $O_2$  would suggest that the V-V intermolecular transfer between these two species is very inefficient, which would lead to each species relaxing at its own V-T rate. This conclusion agrees with the study of Cutler et al.,<sup>13</sup> who found that  $T_{v,N_2}$  and  $T_{v,O_2}$  were quite different in the non-equilibrium flow exiting a Mach 2 heated wind tunnel nozzle.

The error bars in the figure indicate the precision uncertainty (95% confidence) that was determined using repeated measurements. Measurements are presented for radial locations where the signal-to-noise ratios are high enough that accurate fits could be made. In the near field, where there is still a potential core, there is no  $O_2$  in the jet fluid, and so the  $O_2$  Raman signals diminish faster than the  $N_2$  signals as the probe volume is translated toward the jet axis.

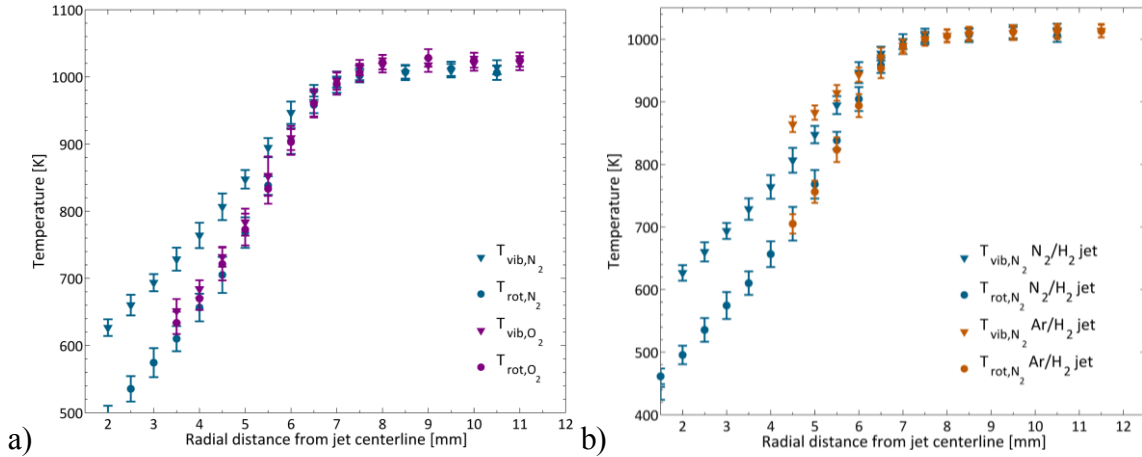


Figure 15: a) Radial trace of N<sub>2</sub> and O<sub>2</sub> temperatures with H<sub>2</sub>/N<sub>2</sub> fuel and b) radial trace of N<sub>2</sub> temperatures with H<sub>2</sub>/N<sub>2</sub> and H<sub>2</sub>/Ar fuel. Measurements were all taken at an axial distance of 2 jet diameters downstream of the nozzle in the pre-flame region.

As with the air-air mixing study, the apparent non-equilibrium strength in the H<sub>2</sub>/N<sub>2</sub> case is reduced by mixing. As previously, the N<sub>2</sub> in the jet is replaced with argon to isolate the hot-to-cold relaxation process as vibrationally cold N<sub>2</sub> is no longer being provided on the high speed side. This effect is illustrated above in Fig. 15b. While the rotational temperatures for the two different jet compositions match well, the measured non-equilibrium is much stronger when there is no longer N<sub>2</sub> present in the jet. Measurements with the H<sub>2</sub>/Ar jet are particularly difficult due to the lack of N<sub>2</sub> from the high-speed side of the shear layer to provide scattered signal; this is why the profile for these runs does not extend as far into the jet.

Values for freestream density and mass entrainment ratios are presented below in Table 4. If more mass from the cold jet is entrained ( $E_m > 1$ ), the mixing layer temperature profile will be depressed such that the hot side will be further from the mean temperature. The hot-to-cold process dominates entrainment in all cases, which agrees with the behavior seen in the experimental shear layer profiles as well as the CFD results.<sup>14</sup> However, the cold-to-hot process is still present and should influence the mean vibrational temperature profiles by reducing the apparent non-equilibrium measured, as seen in Fig. 15b.

Table 4: Calculated shear layer density and mass entrainment ratios

Case	$s$	$E_m$
H <sub>2</sub> /N <sub>2</sub>	1.43	1.67
H <sub>2</sub> /Ar	1.31	1.75
H <sub>2</sub> /CH <sub>4</sub>	2.14	1.37

The temperature profile at a location farther downstream is presented in Fig. 16. This location corresponds to the farthest downstream location where the flame is never present. At this location, the jet potential core is just collapsing as there is no flat section in the temperature profile corresponding to a region of pure jet fluid; therefore, the entire jet width can be probed with Raman scattering since the N<sub>2</sub>-rich outer flow has penetrated to the center of the jet. The

shear layer profiles on each side of the jet show similar behavior to the upstream profiles presented above, which is expected since this location is just beyond the shear layer region of the jet. It is important to note that non-equilibrium will not immediately disappear downstream of this point. The driving force behind non-equilibrium generation is the temperature gradient in the flow, which is still present beyond the potential core. The non-equilibrium will simply decay in magnitude as the jet centerline temperature rises to the outer flow temperature due to downstream turbulent mixing. This behavior is also observed in our simulation results presented in Ref. 14 (see also below) where it is shown there that non-equilibrium at the centerline begins near the collapse of the potential core and continues until far downstream where combustion products have been entrained to the jet centerline.

Temperatures were not extracted from Raman scattering spectra in the region where the flame is intermittently present due to rapid turbulent fluctuations. Owing to the intermittent presence of the flame, these regions have a widely spread bimodal temperature PDF, where the two peaks will be around the freestream (1000 K) and post-flame (2400 K). As seen previously, the Raman fitting procedure will only converge to a meaningful temperature value if the temperature PDF within the measurement volume is sufficiently narrow. However, measurements can be taken downstream of this region. Results at such a downstream station are plotted in Fig. 17. The acquisition of spectra at this axial location required a 15 s integration time. The figure at left shows a mean profile through both sides of the flame, which is seen to be symmetric, as expected. It is also clear that the non-equilibrium, which is seen in the non-reacting regions upstream, is completely gone at the location of peak temperature in the radial profile. This lack of non-equilibrium is expected since a high concentration of flame products such as H<sub>2</sub>O should quickly relax the non-equilibrium. Non-equilibrium is detected at the jet centerline just as it is in the upstream profile of Fig. 16. Our simulation results show a similar non-equilibrium zone at the centerline near the height of the mean flame base. Figure 17b shows a zoomed-in look at the peak temperature location. The peak measured temperature of 1835 K is 240 K less than the adiabatic flame temperature predicted for this fuel, which is reasonable considering the measurement is time-averaged and the flame base fluctuates substantially.

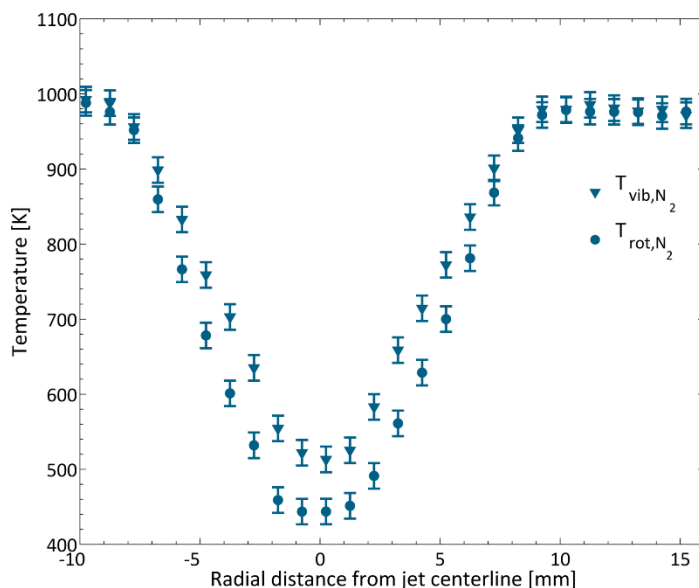


Figure 16: Radial mean profiles of N<sub>2</sub> rotational and vibrational temperature approximately four diameters downstream of the nozzle exit.

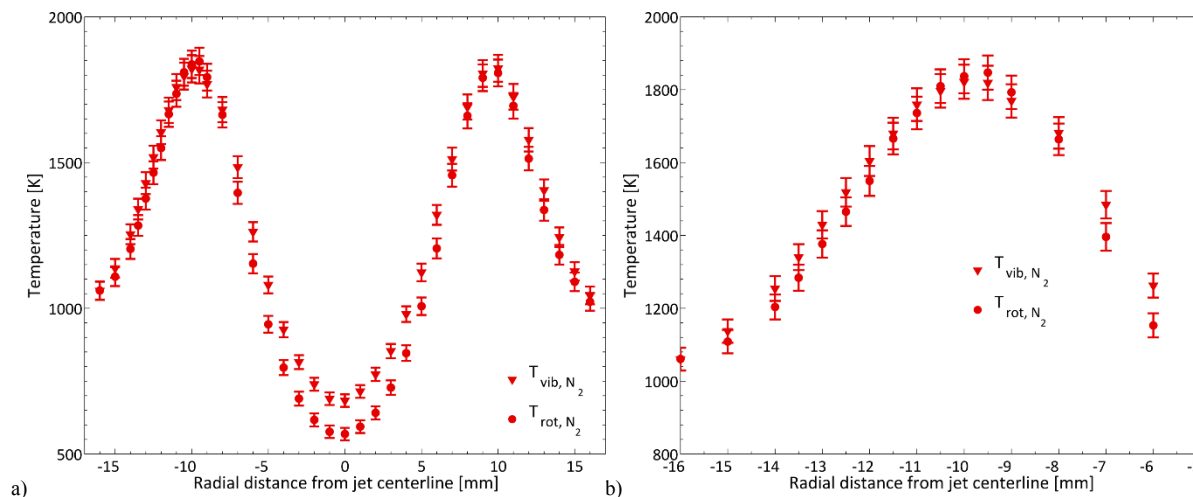


Figure 17: Radial trace of N<sub>2</sub> temperatures 7 diameters downstream of nozzle exit (downstream of flame base) (a) Profile across entire flame, (b) zoomed-in view to show data near the peak temperature

## 2. Theoretical effort

Bimolecular chemical reactions may be dissociation or exchange type and are usually written as  $AB + CD \rightarrow A + AB + CD$  and  $AB + CD \rightarrow AC + BD$  respectively. This description is adequate to describe reaction rates under thermal equilibrium conditions (i.e. Maxwellian velocity distributions and Boltzmann energy distributions for internal states). It must be extended for conditions of thermal non-equilibrium and for dissociation reactions, for example, we must write  $AB(v_1, J_1) + CD(v_2, J_2) \rightarrow A + B + CD(v_3, J_3)$ .

Because the reaction cross-sections are state dependent the overall reaction rate must be obtained by **summing** over all product internal states and **averaging** over reactant internal states:

$$R_f = k_f n_{AB} n_{CD} = n_{AB} n_{CD} \sum_{v_3, J_3} \sum_{v_1, J_1} \sum_{v_2, J_2} \frac{n_{AB}(v_1, J_1)}{n_{AB}} \frac{n_{CD}(v_2, J_2)}{n_{CD}} \overline{\sigma(1, 2 \rightarrow 3, d) c_{rel}}^T.$$

Here the state-specific reaction cross-section (dissociation cross-section in this example) is averaged over the relative speed distribution function, which may be assumed to be Maxwellian except under extreme non-equilibrium conditions:

$$\overline{\sigma(1, 2 \rightarrow 3, d) c_{rel}}^T \equiv \int_0^{\infty} \sigma(1, 2 \rightarrow 3, d) c_{rel} \chi_M(g; T) dc_{rel}.$$

Reaction rates in non-equilibrium flows differ from equilibrium rates because the internal states of the reactants are not described by Boltzmann distributions. One requires state-specific reactions rates for the most detailed description, but this is computationally intractable for reacting flows in complex geometries. Multi-temperature models of reactions are an intermediate description which assumes that internal energy modes, in particular the vibrational modes, are Boltzmann distributed with vibrational temperature  $T_v$ , and  $T_v \neq T_r = T_t$ . Quasi-classical trajectory (QCT) calculations on potential energy surfaces (PESs) determined from ab initio quantum chemistry must be used to determine state-specific rates. Depending on the level of

detail required the initial states of the reactants are sampled over appropriate Boltzmann distributions to obtain suitably averaged rates.

### QCT code development

We have developed and tested a highly scalable parallel algorithm to run QCT trajectories on general PESs. The program is designed to distribute the computational effort over available cores and adjusts the sampling automatically to match a desired global uncertainty as shown in Figure 18. Each process samples many trajectories and inter-process communications are designed as checkpoints. It should be noted that the number of checkpoints is independent of the number of active cores.

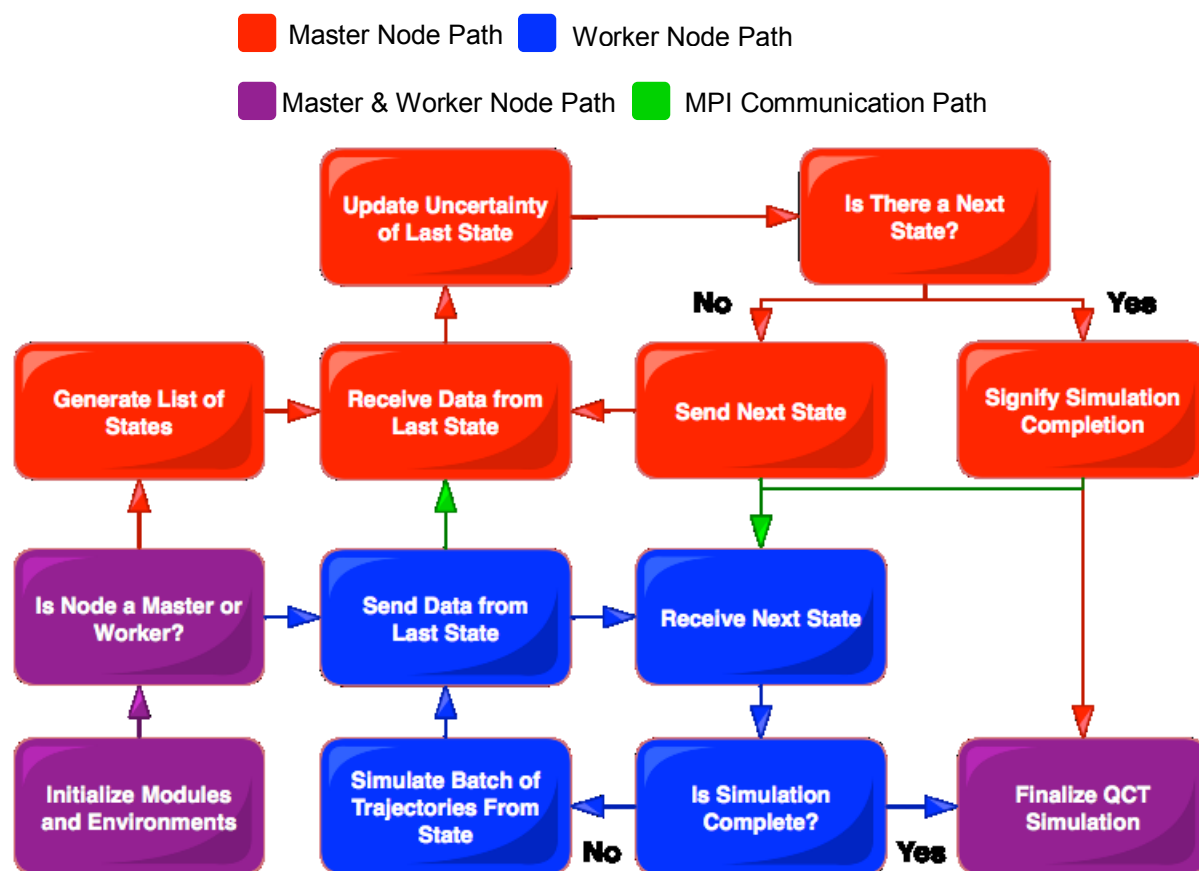


Figure 18. Schematic diagram of program workflow

The program was tested by running 5 million trajectories for the  $N_2+N_2$  system and demonstrated linear scaling of the computational time with the number of active cores.<sup>15</sup> Figure 19 shows the results of two test runs to calculate inelastic cross-sections for  $N_2-N_2$  collisions. For Test A there are 200 trajectories simulated in each iteration i.e. each batch of trajectories. In Test B, there were 800 trajectories per iteration, resulting in a reduction by a factor of four in the number of MPI calls because there are fewer instructions from the master node. The total computational time as a function of the number of processors is shown in Fig. 19a. Both tests show excellent weak-scaling as the number of processors was increased from 24 to 4096, with ~10% increase over the minimum for Test A, and ~4% increase over the minimum for Test B. Figure 19b shows

the variation of the average CPU time per trajectory with the number of trajectories simulated per processor. This plot shows that faster processors generally simulate more trajectories, so slow processors do not act as a bottleneck to the computations.

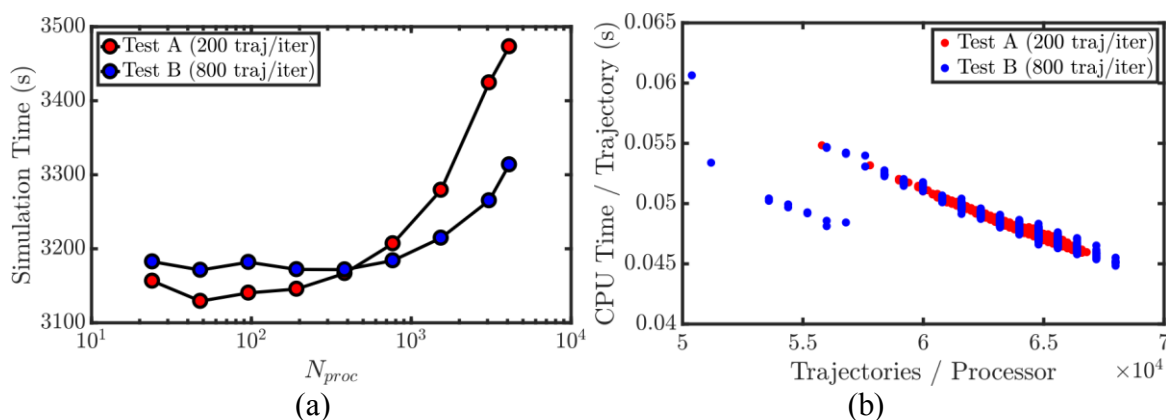


Figure 19. Demonstration of parallel scaling up to 4096 cores for QCT calculations of N<sub>2</sub>+N<sub>2</sub> collisions

### Code verification

The code was verified by simulating 500 million trajectories on the N<sub>4</sub> PES of Paukku et al.<sup>16</sup> and compared to the results of Bender et al.<sup>17</sup> who used the same PES and assumed an internal (ro-vibrational) temperature  $T_{rv}$  that is possibly different from the translational temperature  $T_t$ . In our calculations results were obtained on a relatively coarse grid  $T_t$  and  $T_{rv}$  and interpolated onto a full surface using the interpolation procedure of Wang, et al.<sup>18</sup> The QCT calculations were run with Monte Carlo sampling over initial conditions (orientation of molecules, vibrational phase, etc.). Details are given in the doctoral dissertation<sup>19</sup> of Stephen Voelkel, one of the graduate students supported by this grant. For an initial state  $\xi$  and desired final state  $\xi'$ , with  $N_r$  trajectories resulting in the desired transition out of  $N$  sampled trajectories, then the probability of the transition  $P(\xi \rightarrow \xi') \approx N_r/N$ , and the precision of the estimate improves for large sample numbers. The uncertainty can be expressed quantitatively as:

$$\delta P(\xi \rightarrow \xi') = 2 \frac{N_r}{N} \left( \frac{N - N_r}{N_r (N - 1)} \right)^{1/2}$$

### Selective sampling for increased efficiency

We have developed a new sampling procedure to reduce computational cost when sampling for processes that have low probability of occurring. This is critical to computing reaction rates at modest temperatures (2,000-6,000 K) which are commonly found in engineering applications. For low probability outcomes, the standard Monte-Carlo technique requires a very large number of samples in order to obtain reasonable statistics and corresponding precision on desired outcome. Low probability reactive events correspond to high activation energy processes which require relative translational energies that are only in the high energy tail of the Maxwellian distribution. We have implemented a scheme that only samples trajectories beyond the estimated cut-off, and accounts analytically for all the trajectories that are below the required threshold. Thus the effective number of trajectories can be several orders of magnitude larger than the number of simulated trajectories which greatly increases efficiency.

Figures 20a,b compare the measured convergence rate of the relative uncertainty in the  $N_2$  dissociation rate coefficient for standard sampling and selective sampling. At high temperature (30,000K) the rate coefficient is high and there is no change in the required number of trajectories when using selective sampling. However, at 6,000 K, the dissociation rate is low, and the number of trajectories required to get  $\sim 10\%$  error in the dissociation rate is *reduced by a factor of 100* from  $10^{10}$  to  $10^8$ . The improvement will be even larger at lower temperatures. We believe this efficiency improvement will be very useful when using QCT for many engineering applications.

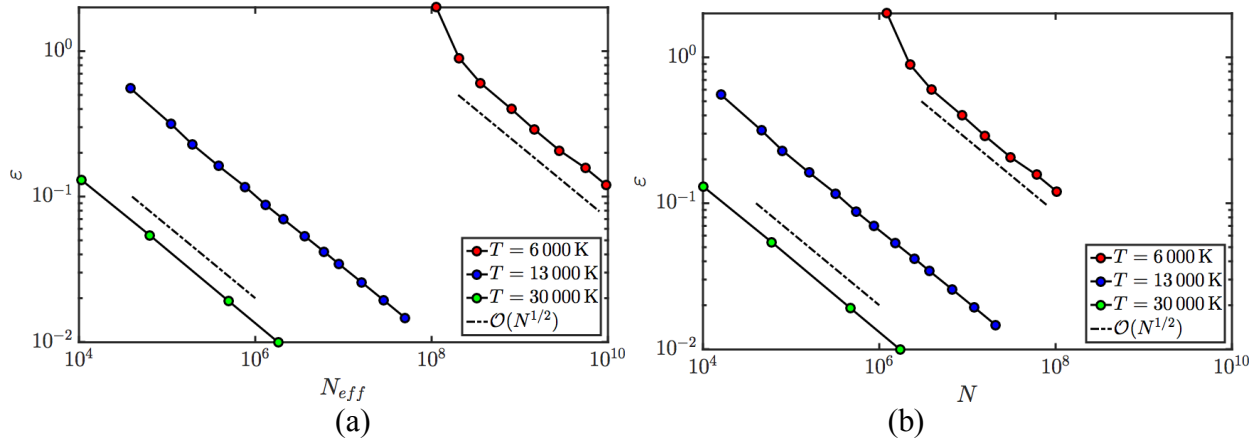


Figure 20. Variation in estimated error of computed  $N_2$  dissociation rate with number of trajectories for (a) Standard sampling and (b) Selective sampling at  $T = 6,000, 13,000,$  and  $30,000$  K.

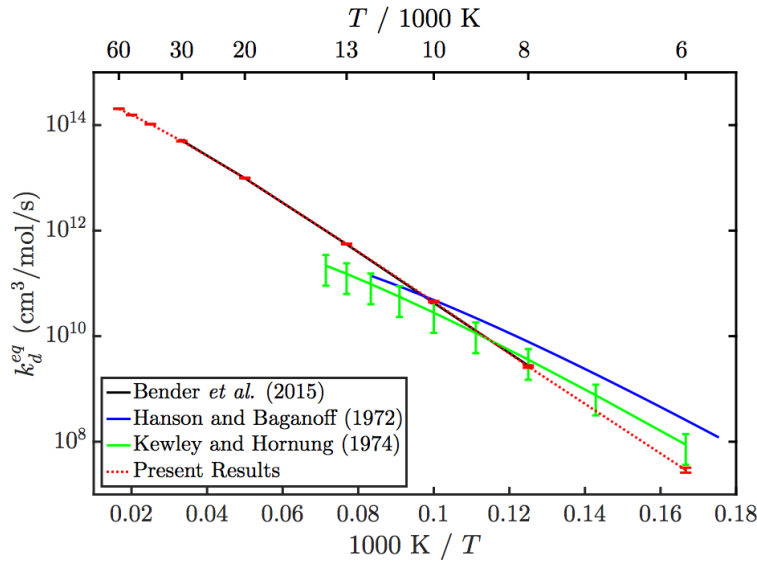


Figure 21. Verification of the QCT code by comparison of our equilibrium results with other calculations and experiment.

Figure 21 compares the thermal equilibrium dissociation rate computed via QCT using selective sampling in the range  $6,000 \text{ K} \leq T \leq 60,000 \text{ K}$ . The uncertainties are small even at 6,000 K because of the selective sampling procedure. Our results are virtually indistinguishable from the QCT results of Bender, et al.<sup>17</sup> in the range  $8,000 \text{ K} \leq T \leq 30,000 \text{ K}$  obtained using the same

potential energy surface. Bender does not use selective sampling and did not present calculations at temperatures below 8,000 K.

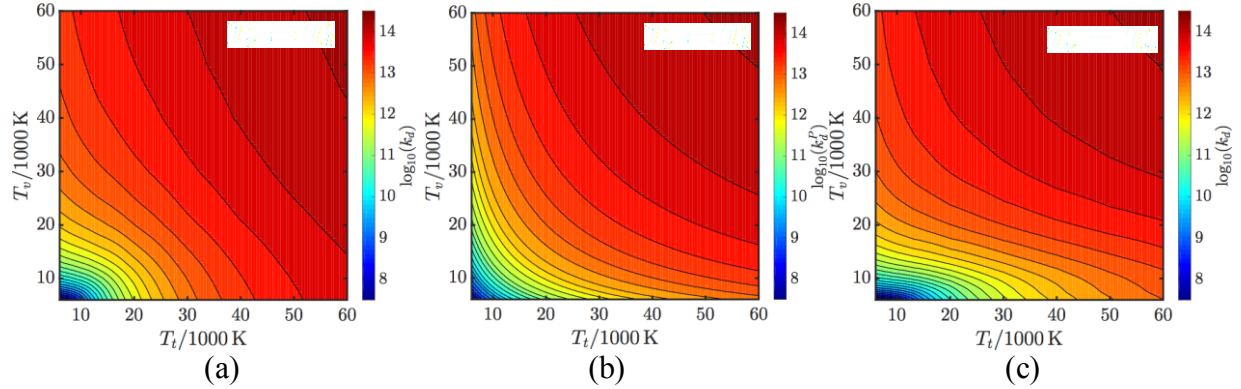


Figure 22. (a) Non-equilibrium  $N_2$  dissociation rate  $k_d(T_t = T_r, T_v)$  computed from QCT code (b) Non-equilibrium rate from Park model. (c)  $k_d(T_t, T_r = T_v)$  computed using the QCT code.

Figures 22 (a) and (b) compare the  $N_2$  non-equilibrium dissociation rate in the range  $6,000 \text{ K} \leq T_t, T_v \leq 60,000 \text{ K}$  computed via QCT and compares the results with Park's model<sup>20</sup>  $k_d^{Park} = k_d^{eq}(T_{eff})$  where  $T_{eff} = \sqrt{T_t T_v}$ . We use  $T_r = T_t$  for the results shown. Note the logarithmic scale on the plots. The two models agree along the diagonal  $T_v = T_t$  by design. It can be seen that Park's model works reasonably well at high temperatures but there are significant discrepancies at low temperatures. Figure 22 (c) shows the non-equilibrium dissociation rate assuming  $T_r = T_v$ . The QCT code has been used to compute the non-equilibrium dissociation rate  $k_d(T_t, T_r, T_v)$  for  $N_2$  and an approximate three temperature rate model is proposed that can be used in CFD codes that currently use Park's model.

$$k_d(T_t, T_r, T_v) = k_d^{eq}(T_e); T_e \equiv T_t^{c_1} T_r^{c_2} T_v^{c_3}; c_1 + c_2 + c_3 = 1.$$

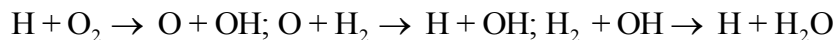
The accuracy of the model is quantified using the root mean square (RMS) of the relative error of the fit, i.e.  $\varepsilon \equiv \left\| \left( k_d^{eq}(T_e) - k_d(T_t, T_r, T_v) \right) / k_d(T_t, T_r, T_v) \right\|_2$ . The fit coefficients for several temperature ranges are given in Table 5. A single fit over the entire temperature range gives results to no better than a factor of 2 (nearly 100% error), but much higher accuracy is possible for restricted temperature ranges that are relevant to re-entry flows.

Table 5: Coefficients for effective temperature model over selected temperature ranges

$T$ range [K]	$c_1$	$c_2$	$c_3$	RMS error (%)
6,000 – 60,000	0.3133	0.2787	0.4080	98.6
13,000 – 40,000	0.3092	0.2258	0.4650	22.0
30,000 – 60,000	0.4692	0.1777	0.3531	2.86

## Hydrogen oxidation reactions

The QCT code was applied to calculate non-equilibrium reaction rates for three key reactions in the hydrogen combustion mechanism:



The potential energy surfaces and other computational details are presented in Voelkel, et al.<sup>21</sup> Non-equilibrium reaction rate coefficients  $k_r(T, T_v)$  for these reactions were computed assuming  $T_r = T_t = T$ . For reaction 3 ( $\text{H}_2 + \text{OH}$ ) we examined the effect of vibrational non-equilibrium of  $\text{H}_2$  and  $\text{OH}$  independently. In order to apply the results conveniently in CFD codes an efficiency function is defined  $\varphi(T, T_v) \equiv k_r(T, T_v)/k_r^{eq}(T)$ . An important conclusion of this study is that exchange reactions of the type studied, are much less sensitive to vibrational non-equilibrium than is predicted by the standard Park model that has often been used in absence of better data. Further the efficiency functions are reaction and species dependent. This can be seen in in Fig. 23 where the efficiency function contours are plotted as a function of  $T_v/T$  and  $T$  for the reactions above.

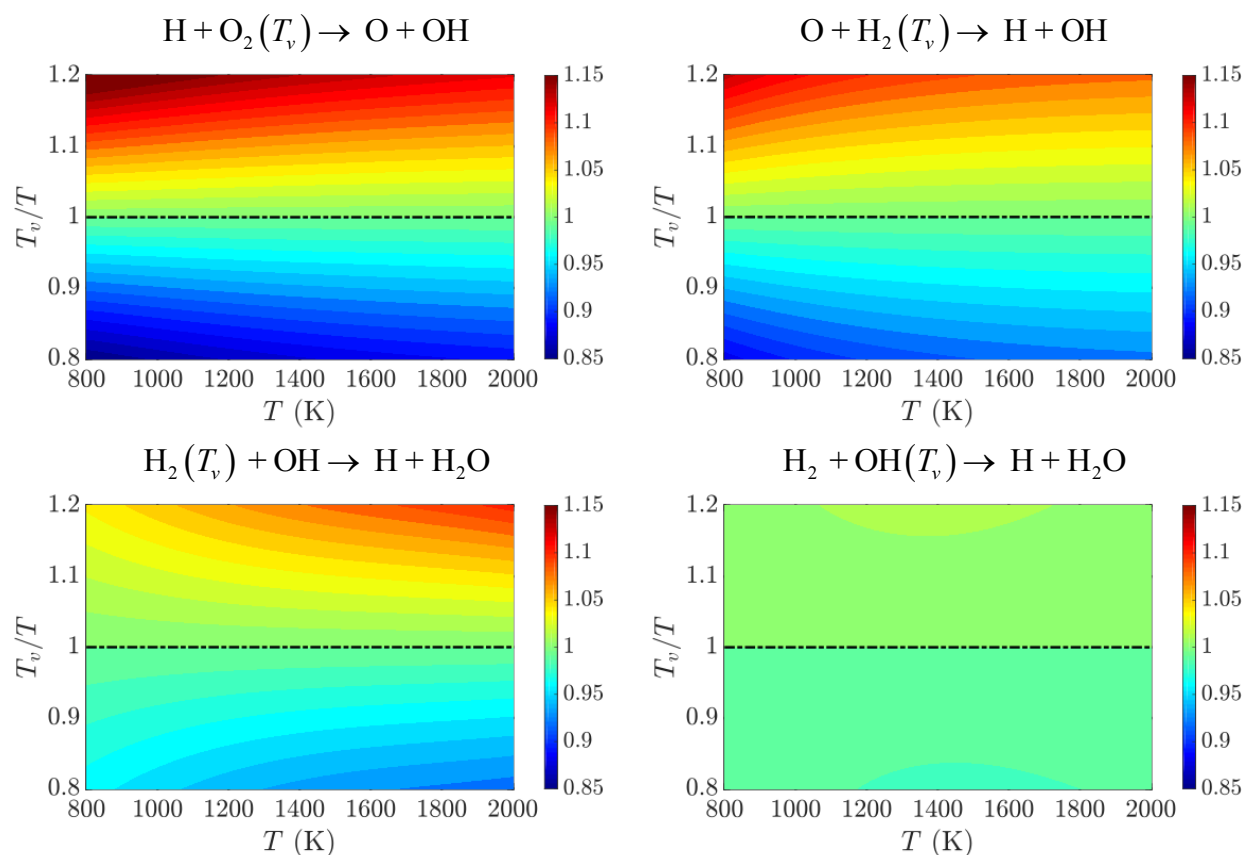


Figure 23. Contour maps of the efficiency function showing dependence on  $T_v/T$  and  $T$  for key hydrogen combustion reactions.

While there is generally an enhancement in the reaction rate ( $\varphi > 1$ ) when  $T_v > T$ , the magnitude depends on the reaction. The first two reactions are more sensitive to vibrational non-equilibrium at low  $T$ , while the  $\text{H}_2 + \text{OH}$  reaction is more sensitive to vibrational non-equilibrium of  $\text{H}_2$  at high  $T$ , and is very insensitive to vibrational non-equilibrium of  $\text{OH}$ .

Figure 24 shows the efficiency surfaces for these reactions as a function of  $T$  and  $T_v$  in red. The QCT results are compared to the efficiency that would be obtained using the standard Park model (blue surfaces) and the coupled vibration chemistry vibration (CVCV) model (aqua

surfaces) that was developed by Knab et al.<sup>22,23</sup> to describe non-equilibrium chemistry for hypersonic flows. In order to facilitate use of these results in standard CFD codes, we fit the QCT surface to an “optimized” Park-type model,  $\varphi(T, T_v) = k_{eq}(T_{eff})/k_{eq}(T)$ ;  $T_{eff} \equiv (TT_v^\zeta)^{1/(1+\zeta)}$ .

The standard Park model corresponds to  $\zeta = 1$ . Neither the CVCV model nor the standard Park model matches the QCT calculations well. The optimum value of  $\zeta$  for these exchange reactions is less than 0.2, and the particularly low value  $\zeta_{opt}$  for the  $H_2 + OH(T_v)$  reaction reflects how insensitive the rate coefficient is to vibrational non-equilibrium of OH. Table 6 shows the RMS errors of the model efficiency surfaces relative to the QCT values.

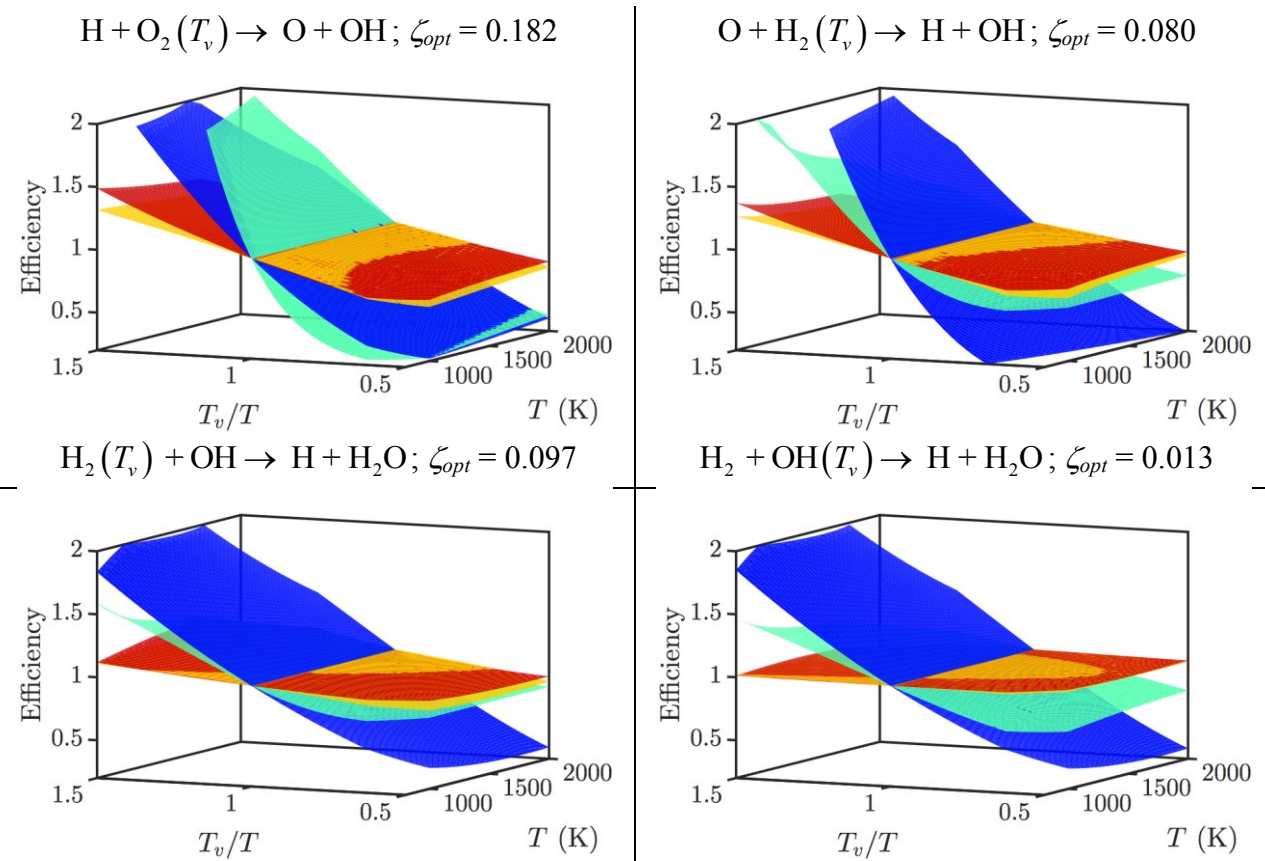


Figure 24. Efficiency function surfaces as a function  $T_v/T$  and  $T$  for key hydrogen combustion reactions. Red – QCT computation; Cyan – CVCV model; Blue – Standard Park model; Yellow – Optimized Park-type fit to QCT calculated surface.

Table 6: RMS error of the modeled efficiency functions compared to the QCT results

$T$ range [K]	$\zeta_{opt}$	This work $k(T, T_v) = k_{eq}(T_{eff})$ $T_{eff} \equiv (TT_v^{\zeta_{opt}})^{1/(1+\zeta_{opt})}$	Original Park	CVCV
H + O <sub>2</sub> ( $T_v$ )	0.182	0.012	0.211	0.283
O + H <sub>2</sub> ( $T_v$ )	0.080	0.010	0.435	0.108
OH( $T$ ) + H <sub>2</sub> ( $T_v$ )	0.097	0.016	0.242	0.047
OH( $T_v$ ) + H <sub>2</sub> ( $T$ )	0.013	0.003	0.306	0.107

In addition to the purely empirical two-temperature fit described above, we have generated a more physics based species-specific efficiency function similar to the model presented by Aresntiev et al.<sup>24</sup> This is based on the forward and reverse activation energy of the reaction as well as the initial and final vibrational energy of the products and reactants, respectively. For a specific reaction, we define the analytical state-dependent efficiency function:

$$\hat{\phi}(v, v'; T) \equiv c_1(T) \exp \left( c_2(T) \frac{\varepsilon_v^+(v) - \max(\varepsilon_v^-(v') - \varepsilon_a^-, 0)}{kT} \right),$$

where  $\varepsilon_v^+(v)$  and  $\varepsilon_v^-(v')$  are the vibrational energy of the reactants and products, respectively,  $\varepsilon_a^-$  is the activation energy of the reverse reaction,  $k$  is the Boltzmann constant,  $c_1(T)$  is chosen so that  $k(T; T_v = T) = k_e(T)$ , and  $c_2(T)$  is a free parameter set to  $(0.6 - T/10^4)$  based on QCT calculations.

From the state-specific function  $\hat{\phi}(v, v'; T)$  we can calculate suitably summed and averaged efficiency functions,  $\hat{\phi}(v; T) = \sum_{v'} \hat{\phi}(v, v'; T)$  and  $\hat{\phi}(T, T_v) = \sum_v f_v(v, T_v) \hat{\phi}(v; T_v)$ , where  $f_v(v, T_v)$  is the fractional population in state  $v$  computed assuming a Boltzmann distribution at  $T_v$ .

The state-specific model  $\hat{\phi}(v; T)$  was compared to  $\varphi(v; T)$  determined directly from QCT calculations for the reaction H + O<sub>2</sub>( $v = 0; 1; 2; 3; 4; 5$ ) → O + OH using the PES developed by Melius and Blint<sup>25</sup> as distributed on POTLIB.<sup>26</sup> Approximately 14 million trajectories were simulated, with more trajectories simulated at low-probability states to minimize the uncertainty (defined as two standard deviations from the mean). Figure 25 shows the proposed model compared to the QCT results. The proposed model closely matches the QCT results, especially as  $T$  increases. The model is not a good match for high  $v$  at low  $T$ . However, the population fraction  $f_v$  of high-lying  $v$  is very small at low  $T$  so the departure from the model fit has little effect on the temperature dependent efficiency function.

The temperature-dependent model  $\hat{\phi}(T, T_v)$  was compared to the standard  $T$ - $T_v$  model of Park<sup>20</sup> and the CVCV model<sup>23</sup> for two of the reactions in the hydrogen-air combustion mechanism: H+O<sub>2</sub>( $T_v$ ) → O+OH and O + H<sub>2</sub>( $T_v$ ) → H + OH. Additionally, these models were compared to  $\varphi(T, T_v)$  directly calculated via QCT as described above. The resulting plots are very similar to

those shown in Fig. 24 above. For both reactions, the QCT results show that vibrational nonequilibrium has a smaller effect than the Park's model and the CVCV model for both  $T_v > T$  and  $T_v < T$ . Overall, the physics-based model  $\hat{\phi}(T, T_v)$  matches the QCT results better than the Park model and the CVCV model except when  $T_v > T$  and  $T < 1400$  K for the reaction  $\text{H} + \text{O}_2(T_v) \rightarrow \text{O} + \text{OH}$ , where Park's model is closer to the QCT results.

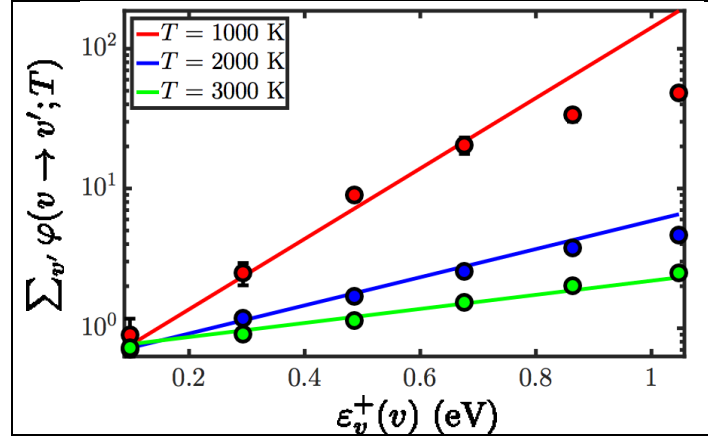


Figure 25. Vibrational energy exchange probability as a function of  $T$  and  $T_{v,\text{O}_2}$  or  $T_{v,\text{N}_2}$ .

We also made QCT calculations of the probability of V-V transfer rate between  $\text{N}_2$  and  $\text{O}_2$  using the  $\text{N}_2\text{O}_2$  potential energy surface from POTLIB. These calculations were motivated by the jet flame experiments described in Section 1, which showed that in the turbulent mixing layer upstream of the flame base, the vibrational temperature of oxygen equilibrated rapidly with the translation-rotational temperature, but the vibrational temperature of nitrogen remained out of equilibrium (see Fig. 15a above). Simulations of this flow using  $P_{VV} = 10^{-2}$  (the value of vibrational energy exchange probability from the standard CVCV model) did not reproduce the experimental data. Simulations (described in Section 3 below) were run with smaller values of  $P_{VV}$  and best agreement was found for  $P_{VV} \cong 10^{-4}$ . The results of the QCT calculations shown in Fig. 26 confirm that in the temperature range of the experiment (500 – 1000 K) the vibrational exchange probabilities are indeed of the order  $10^{-4}$ .

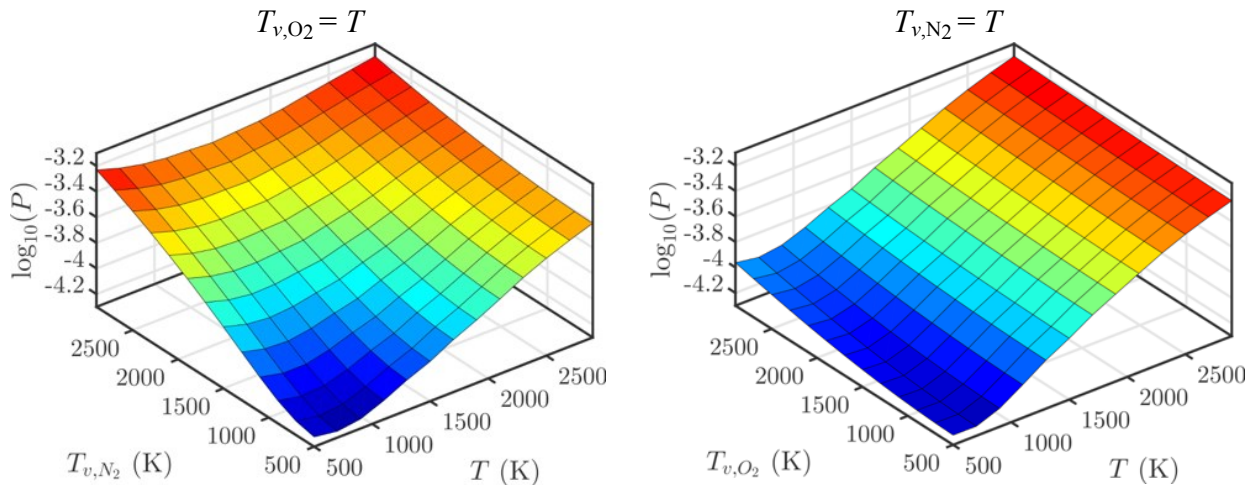


Figure 26. Vibrational energy exchange probability as a function of  $T$  and  $T_{v,\text{O}_2}$  or  $T_{v,\text{N}_2}$ .

### 3. Computational effort

Computations for this project involved both LES and DNS flow simulations of the experimental configuration, a model of a scramjet combustor (Hyshot-II), and also of detonation waves. We have reported on a number of simulations in interim reports which have appeared in several publications. Here we report on simulations performed in the final year of the grant.

#### Simulations of the experimental set-up

Detailed computations of a fuel jet were undertaken to support the experimental effort. The computational domain is shown schematically in Figure 27. The fuel nozzle diameter ( $D$ ) was 8 mm, the coflow diameter was 100 mm to match the experiment. The flow Reynolds number  $Re_d = 32,000$  and the axisymmetric LES spatial grid used was  $(N_x, N_r, N_\theta) = (392, 320, 16)$ .

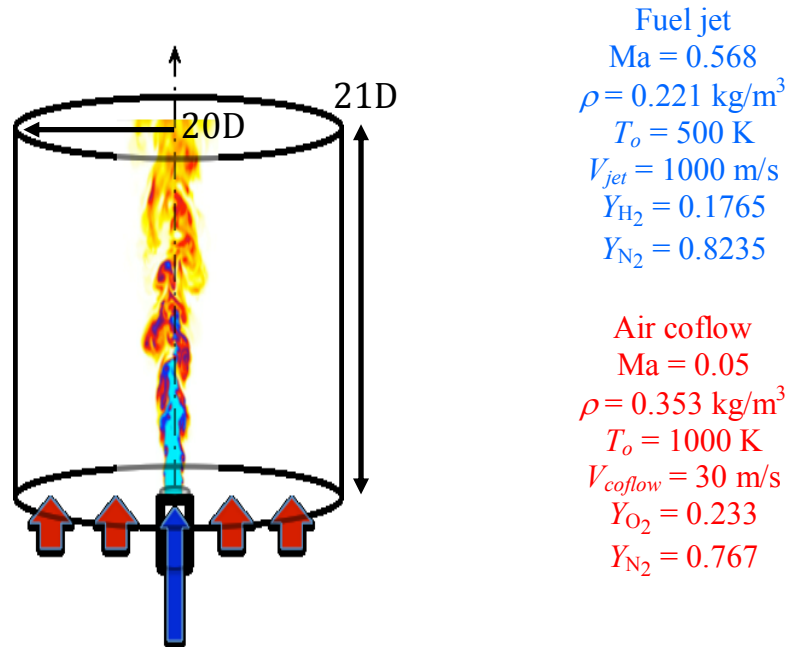


Figure 27. Schematic diagram of the geometry and flow parameters used in LES flow computations

The UTComp compressible flow solver uses a fifth-order WENO scheme with characteristic reconstruction to compute the nonlinear momentum terms, while a fourth-order central scheme is used for the diffusion terms.<sup>27,28,29,30,31,32</sup> The computational time step was 50 ns. The vibrational temperature of each species is tracked independently. The standard Millikan and White correlation<sup>33</sup> is used to model V-T relaxation. The chemistry was modelled using the 9-species, 19-step mechanism of Mueller, et al.<sup>34</sup> We use the QCT derived rates for the three key reactions as described in the previous section. For the remaining 16 reactions in the mechanism we use the CVCV model of Knab, et al.<sup>23</sup> We also use the QCT derived rates for  $N_2$  dissociation, though this reaction is not significant for these flow conditions. The simulation was run for 8 hours on 2000 cores with a CFL number of 0.9. Figure 28 shows sample results for instantaneous translational temperature, and  $N_2$  vibrational temperature obtained from the LES computations. The computed flow is more lifted than observed experimentally because the co-flow velocity used in the simulation (30 m/s) was higher than the experimental value of  $\sim 1$  m/s. Stable numerical solutions could not be obtained for a very low co-flow velocity.

The computations could not reproduce the different profiles of mean vibrational temperatures of  $N_2$  and  $O_2$  observed experimentally (See Fig. 15a above) when using  $P_{VV} = 10^{-2}$  for the CVCV model as in Knab, et al.<sup>23</sup> Because the Knab model was developed for reentry flows at much higher temperatures, we varied the value of  $P_{VV}$  until a good match was obtained between the computed mean profiles and the experimental data. Because of the difference in freestream velocity between experiment and simulation we compare mean profiles by normalizing downstream distance by the potential core length, and the data are presented in scaled variables: temperatures are normalized by the temperature difference between jet and coflow freestreams, and radial distances are normalized by the shear layer width. Figure 29 shows the computed mean profiles for several values of  $P_{VV}$  and superposed on the experimental data measured 2 jet diameters downstream of the nozzle exit. As expected, the difference between the vibrational temperature profiles of  $O_2$  and  $N_2$  increases as  $P_{VV}$  decreases until  $P_{VV}$  is less than  $10^{-4}$ , with little change thereafter. Figure 30 shows profiles of  $T_{v,N_2}$  and  $T_{r,N_2}$  measured 4 diameters downstream of the jet exit, just upstream of the flame base (see Fig. 16). The computed mean profiles of  $T$  and  $T_{v,N_2}$  for this location are superposed on the data for  $P_{VV} = 10^{-2}$  and  $10^{-4}$ . Again, the agreement between data and experiment is greatly improved when  $P_{VV}$  is reduced to  $10^{-4}$ . This comparison between computations and experiment and experiment motivated the QCT study of VV transfer between  $N_2$  and  $O_2$  described in the previous section. As noted above (See Fig. 26) the QCT calculations indicate that  $P_{VV} < 10^{-4}$  for these flow conditions.

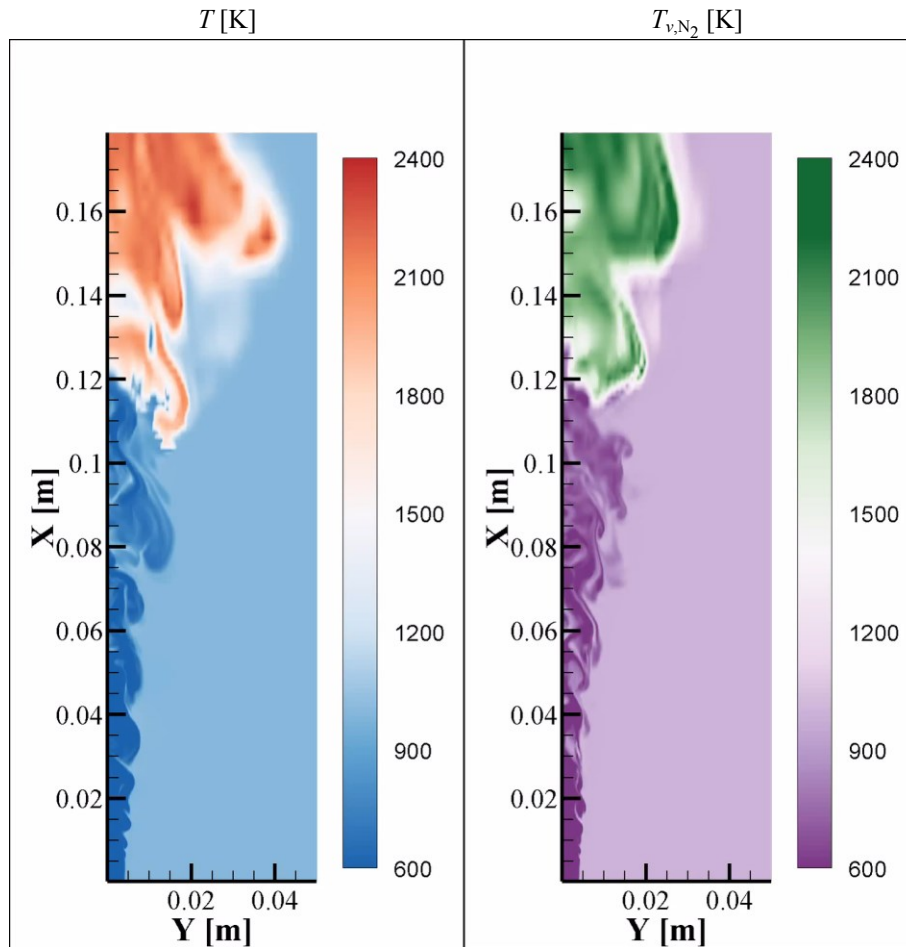


Figure 28. Sample results from LES: Instantaneous (left) translational temperature  $T$ ; and (right)  $N_2$  vibrational temperature,  $T_{v,N_2}$

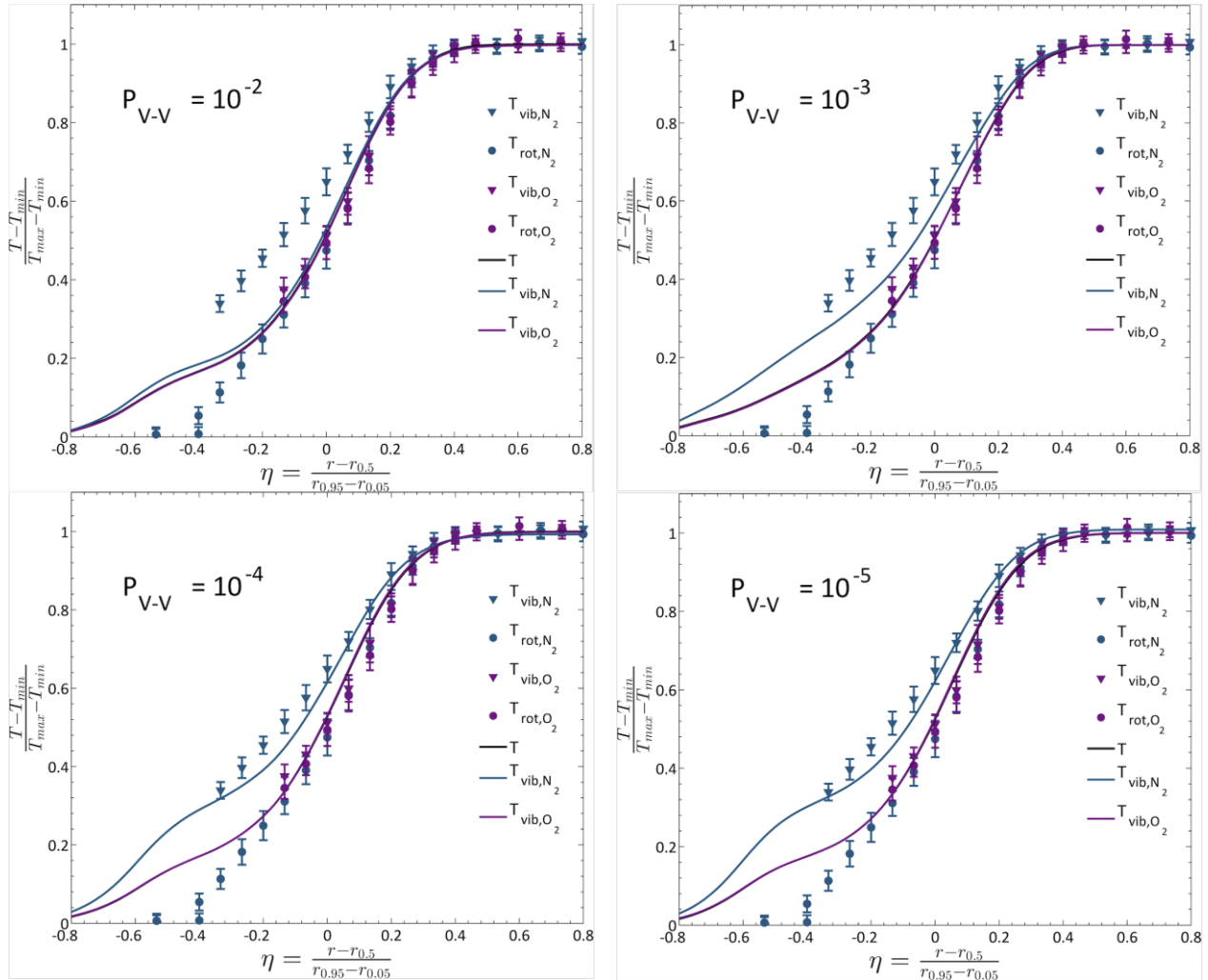


Figure 29. Comparison of experimentally measured profiles of mean  $T_{r,N_2}$ ,  $T_{r,O_2}$ ,  $T_{v,N_2}$ ,  $T_{v,O_2}$  2 jet diameters downstream of the nozzle exit with computed mean values at the same location for different values of  $P_{V-V}$ . Rotational temperatures are in equilibrium with each other and with translational temperature measured by Rayleigh scattering. Good agreement for  $P_{V-V} = 10^{-4}$  with little change in the profiles if the value is reduced further.

Detailed computations were performed on the Hyshot II configuration to implement the non-equilibrium reaction rates determined from the QCT calculations in a more realistic scramjet configuration mimicking high altitude flight at Mach 8. Figure 31 shows the geometry consisting of an  $18^\circ$  ramp leading to the isolator and combustor. Two different cases, with and without thermal nonequilibrium, are simulated. The computational domain is divided into two parts, with the initial bow shock created by the wedge simulated using a standard RANS solver. For the equilibrium condition, the solver directly provides the post-shock conditions based on a shock capturing scheme. For the nonequilibrium case, the vibrational temperature through this shock is frozen while the translational temperature is allowed to increase in order to preserve total energy. The computational domain starts further downstream at  $x = 0$  cm, and extends to  $x = 36.5$  cm.

The far-field pressure is 1197 Pa with air density of  $0.014 \text{ kg/m}^3$ , while the far-field temperature is set to 300 K. The flow over the wedge is first computed using a RANS model to estimate the turbulent boundary layer height and momentum thickness over the wedge section. These values are used to create inflow conditions for the main simulation domain based on a separate DNS of a periodic turbulent boundary layer. The inflow data is collected from this auxiliary DNS calculation and fed to the actual simulation domain used in this work. The Reynolds number based on the inflow boundary layer height is 18,800 at Mach 4.2 (post-shock). For the nonequilibrium case, the flow behind the first bow shock is modified to incorporate the differences in vibrational and translational temperature using the 1D conservation equations with V-T relaxation. In this way, the inflow to the computational domain contains the same internal energy for both cases. A bleed section is introduced, similar to that in the experimental configuration, to naturally remove any additional shock reflections in the combustor section. The bleed is located in such a way that for the flow Mach number considered, the foot of the reflected bow shock is captured by the bleed inlet. The RANS simulation for the wedge section is performed using a realizable  $k-\varepsilon$  model on FLUENT running on 8 processors over a 2D orthogonal grid of  $(n_x, n_y) = (2048, 512)$  until convergence is reached (scaled residuals less than 0.001). The high-resolution calculations are performed using the compressible flow solver UTComp described briefly above. For these calculations a CFL number of 0.85 is used for a time step of 3.9 ns.

The computational domain has over 33 million nodes with a wall-normal refined grid of  $(n_x, n_y, n_z) = (2048, 128, 128)$ . The walls are assumed isothermal at 300 K, with periodic boundary conditions in the spanwise ( $z$ ) direction. The grid size is  $\Delta_z = 16 y^+$ . In the ramp section  $\Delta_x = 18 y^+$  and  $\Delta_y = [1:17]y^+$ , with  $y^+$  estimated to be  $\sim 10 \text{ }\mu\text{m}$ . A preliminary RANS calculation is performed on the forward portion of the wedge, and the turbulent boundary layer on the wedge is computed from an auxiliary DNS computation with  $Re = 18,800$ . The viscosity is determined using Sutherland's law while thermal diffusivity is obtained from a constant Prandtl number of 0.7. Both cases were carried out on 4000 processors using MPI-based parallelization for roughly 120 wall-clock hours. The centerline averaged flow-through time is  $\tau_c = 160 \text{ }\mu\text{s}$ , and the statistics were sampled over  $4\tau_c$  after reaching statistical stationarity. We confirmed that longer averaging did not change the statistics significantly.

The resolution of the simulations was based on the reaction layer thickness. Note that for the turbulent flow conditions, a DNS will require another order magnitude increase in computational mesh, purely based on isotropic turbulence scaling. However, this geometry has two differences. First, the reactions are sufficiently slow in the ignition region so that reaction layers are reasonably broad. For instance the OH layers are resolved using 2-4 grid points for the computational grid used, even at highly strained conditions. Second, the main turbulence generation is through the interaction of the lower velocity fuel jet and the crossflow. Here, the evolution of the mixing/shear layer determines the small-scale structure. In such jet-in-crossflow problems, the fully-developed turbulence structure is not established until further downstream. Hence, the small scales are bound to be larger compared to isotropic turbulence scaling. This is further verified by the size of the reaction zones. Further details are given in Fiévet, et al.<sup>35,36</sup>

The simulations show that vibrational non-equilibrium persists to the combustor inlet. Excited vibrational states are underpopulated and in consequence the translational temperature is higher than in an equilibrium flow. Figure 32 shows the mean temperature profiles on the centerline,

showing that the translational temperature in the non-equilibrium flow is 300 K higher than if the flow were in equilibrium (1600 K instead of 1300 K).

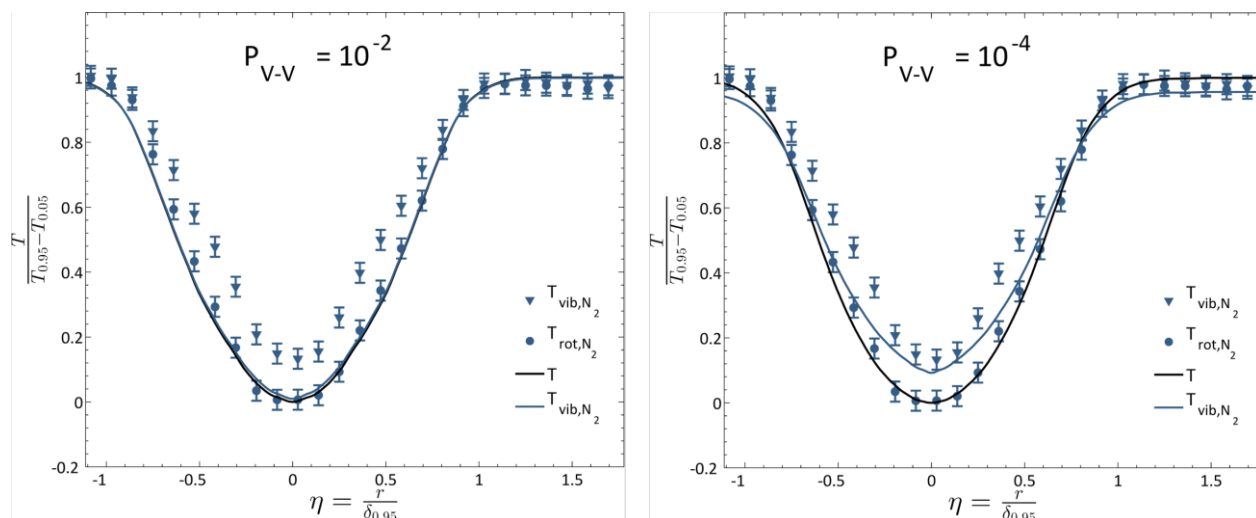


Figure 30. Comparison of experimentally measured profiles of mean  $T$ ,  $T_{v,N_2}$  4 jet diameters downstream of the nozzle exit with computed mean values at the same location for different values of  $P_{V-V}$ . The measured  $T_{r,N_2}$  matches well with computed translational temperature (and temperature measured by Rayleigh scattering). Computed mean profile of  $T_{v,N_2}$  does not agree with experiment for  $P_{V-V} = 10^{-4}$ ; better agreement for  $P_{V-V} = 10^{-2}$ .

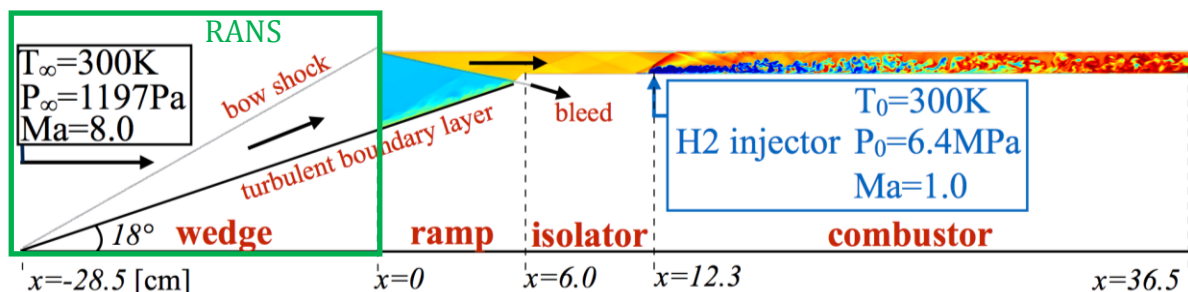


Figure 31. Hyshot II geometry being simulated

The effect of this elevated translational temperature on the three hydrogen reaction studied above is shown in Table 7, and it can be seen that the equilibrium rate coefficients for reactions 2 and 3 are significantly enhanced at the higher temperature. The nonequilibrium rate is given by  $k(T, T_{v,i}) = \varphi(T, T_{v,i}) k_{eq}(T)$ . Figure 32 shows that  $\varphi$  is not very sensitive (<15%) to variations in  $T_v$  for exchange reactions at these conditions. Hence it does not completely offset the augmentation of the reaction rate coefficient by the higher translational temperature. Thus, for these flow conditions, we have the surprising and non-intuitive result that the key reaction rates are higher in the non-equilibrium flow than in an equilibrium flow. Figure 33 shows that the heat release occurs further upstream in the non-equilibrium flow and the flame is stabilized further upstream.

Table 7: Comparison of the equilibrium rates at 1600 and 1300 K

#	Reaction	$k_{eq}(1600\text{ K})/k_{eq}(1300\text{ K})$
1	$\text{H} + \text{O}_2 \rightarrow \text{O} + \text{OH}$	$\sim 1$
2	$\text{O} + \text{H}_2 \rightarrow \text{H} + \text{OH}$	1.23
3	$\text{OH} + \text{H}_2 \rightarrow \text{H} + \text{H}_2\text{O}$	1.45

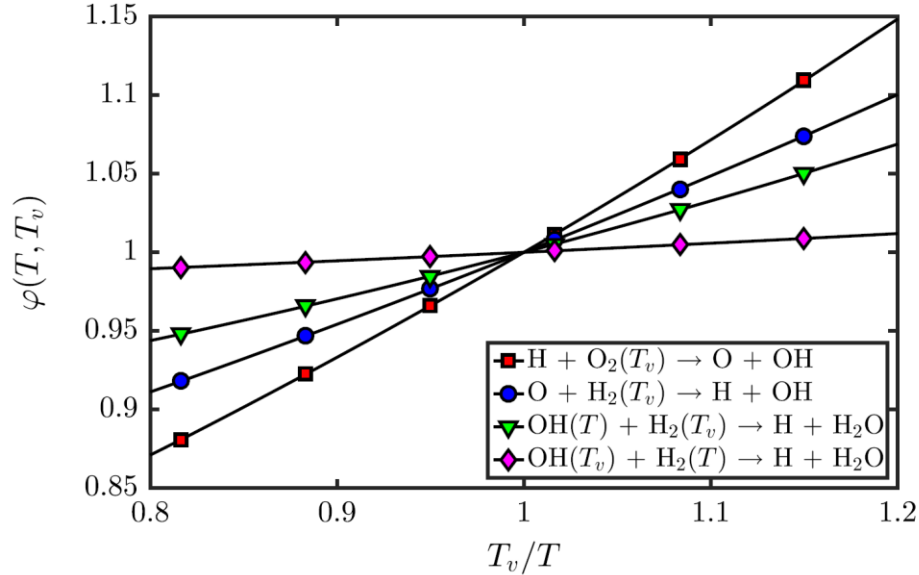


Figure 32. Variation of the efficiency factor for reactions 1-3 (Table 7) at 1200 K.

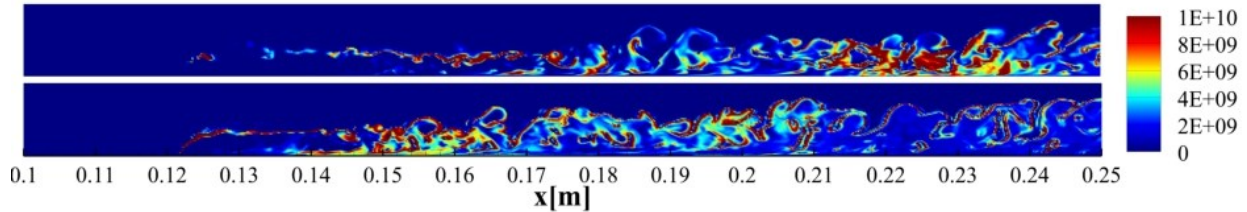


Figure 33. Instantaneous heat release rate ( $\text{W}/\text{m}^3$ ) computed for (top) equilibrium flow, and (bottom) non-equilibrium flow simulations of the Hyshot II combustor. Hydrogen injection is at  $x = 0.123\text{ m}$  (see Fig. 31).

Since each species is described by a specific vibrational temperature, it is interesting to see the evolution of these vibrational temperatures as the flame stabilizes. Figure 34 shows that there are significant differences between the relaxation rates of the vibrational temperatures of individual species.  $\text{O}_2$  exhibits nonequilibrium at the jet inlet due to the inflow conditions, but is quickly equilibrated when the initial chemical reactions that produce  $\text{H}_2\text{O}$  occur. This is similar for  $\text{H}_2$ , which exhibits significant nonequilibrium during the expansion process close to the injection point. The vibrational temperature of  $\text{H}_2\text{O}$  shows only a small region of high vibrational temperatures, before quenching to near-equilibrium values. It is important to note that the flow away from the reaction zone still contains substantial nonequilibrium due to the presence of  $\text{N}_2$ . Hence, collisions with  $\text{N}_2$  molecules transfer nonequilibrium to other species. Further details are given in Ref. 35.

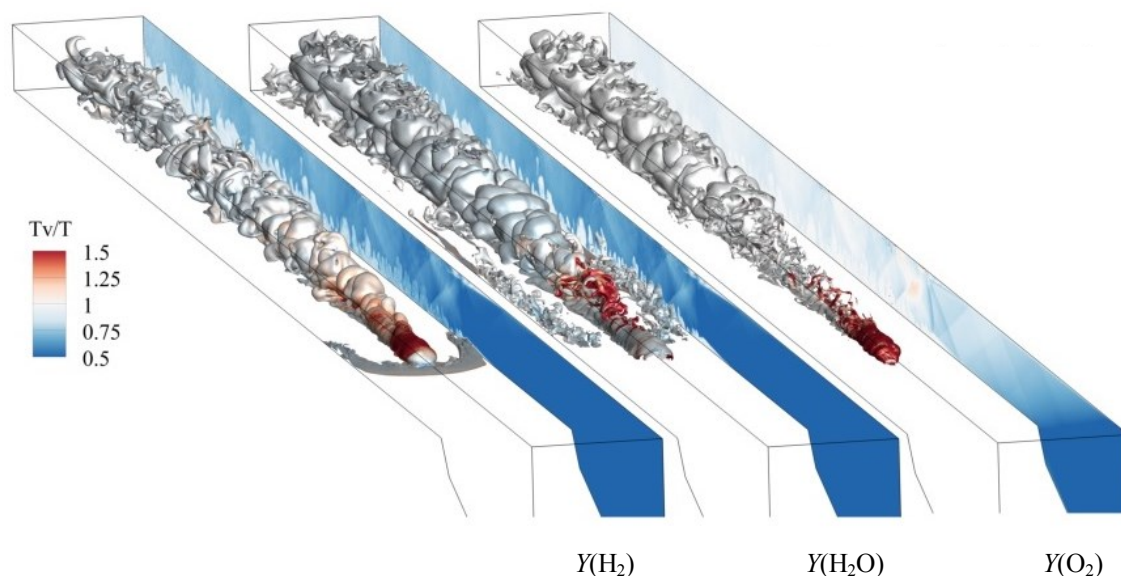


Figure 34. Isocontours of mass fraction  $Y_x = 0.1$  for (left)  $H_2$ , (middle)  $H_2O$ , and (right)  $O_2$ . In each case the mass fraction contour is colored by the ratio of species vibrational temperature to gas translational temperature. The ratio  $T_{v,x}/T$  for each species on the symmetry plane is also shown. Note that the low ratios for  $H_2$  and  $H_2O$  in the inlet and isolator far upstream of the injection point are not meaningful as there is no significant concentration of these species far upstream.

#### 4. Summary and Conclusions

There has been a fruitful interaction between experiment, theory, model development, and numerical simulations under this grant. High dispersion time-averaged Raman scattering measurements were used to identify persistent vibrational non-equilibrium of nitrogen in high-speed shear layers with mismatched gas compositions. Mixing-induced thermal non-equilibrium was detected in the shear layer upstream of the turbulent hydrogen flame in  $N_2$  but not  $O_2$ . Rotational temperatures of the two species agree to within the measurement precision. As expected, the non-equilibrium is relaxed immediately beyond the average flame-base location due to the presence of combustion products. The presence of non-equilibrium is confirmed using Rayleigh thermometry images to quantify the effect of translational temperature variation in the Raman measurement volume. These results were compared to large-eddy simulations with vibrational relaxation effects to study the effect of interspecies vibrational energy transfer models. The measurements and average simulated temperature fields could only be made to agree when the interspecies vibrational coupling is very weak. This required a two order of magnitude change in the probability of VV transfer that was widely used in simulations of non-equilibrium flow.

A highly efficient QCT code was developed under this grant and was used to determine non-equilibrium reaction rate coefficients for three key reactions in the hydrogen combustion mechanism. It was also used to verify the experimentally observed slow V-V transfer between nitrogen and oxygen, which allows for persistent vibrational non-equilibrium prior to production of water with consequent rapid vibrational relaxation. Simple empirical fits were used to implement these QCT based non-equilibrium rates into numerical flow simulations. An improved physics-based model was also developed, that shows promise, but requires further development.

Simulations of the flame from a high-speed jet in a heated co-flow showed that vibrational non-equilibrium delayed flame ignition. However for hydrogen injected in cross-flow in a shock heated air stream as in a scramjet, the persistent nitrogen non-equilibrium leaves the air at an elevated translational temperature and was found to move ignition upstream resulting in a more stable flame. This demonstrates that one can devise geometries where non-equilibrium can be used to advantage to stabilize a flame in a scramjet.

Key insights arising from this work relative to scramjet design are

- $N_2$  vibrational nonequilibrium plays a significant role in determining ignition delay (and hence flame stability) under scramjet combustor conditions
- The nonequilibrium effect can either advance or delay ignition relative to equilibrium flow
- Effect arises principally from impact of vibrational nonequilibrium on translational temperature, with consequent effect on reaction rates
- Direct effect of nonequilibrium  $T_v$  on rate coefficients is small at scramjet conditions because the key reactions are exchange reactions rather than dissociation reactions
- The nonequilibrium can be controlled via strength of shocks and expansions, and location of fuel injection relative to these flow features

## 5. Future Work

The experimental work in the high speed jet should be extended to enable single-pulse collection of Raman vibrational spectra. A multi-pass laser configuration, with a higher energy laser pulse should enable single pulse measurements of vibrational temperature using high dispersion Raman spectroscopy. It is unlikely that rotational temperature can be obtained via single pulse measurements, because the O- and S- branches that show resolved rotational structure are much weaker than the Q-branch. Additional measurements to advance the fundamental understanding of non-equilibrium flows and processes will require a facility that operates continuously so reliable measurements can be made of high-lying states with very small populations. An inductively coupled plasma torch is an ideal facility for such experiments as it produces a steady high temperature flow with no electrode contamination.

The QCT code is highly parallel and can produce state-specific and suitable state-average cross-sections and rate coefficients from an available potential energy surface (PES). Currently, the bottleneck is production of the PES from *ab initio* quantum chemistry calculations and generation of suitable fits to the high-dimensional PES. The solution of challenging engineering problems under extreme conditions that are of interest to the Air Force, would be greatly facilitated if the PES could be adaptively generated during the course of the QCT calculations. Additionally, it would be very useful if quantitative metrics could be developed to specify *how accurately* the PES must be determined, and *in what regions* of the high dimensional space it must be known accurately. Presently, the fits to the PES are determined by experts, and the metrics used often focus on reproducing static, equilibrium properties, and there is no simple way of relating this to accuracy in chemical dynamics calculations. A research effort in this area is needed to improve the state-of-the art.

## 6. References

1. Barlow, R. S., Fourguette, D. C., Mungal, M. G., and Dibble, R. W., "Experiments on the structure of an annular compressible reacting shear layer," *AIAA J.* **30**, 1992, pp. 2244-2251.
2. Cabra, R., Myhrvold, T., Chen, J. Y., Dibble, R. W., Karpetis, A. N., and Barlow, R. S., "Simultaneous laser Raman-Rayleigh-LIF measurements and numerical modeling results of a lifted turbulent H<sub>2</sub>/N<sub>2</sub> jet flame in a vitiated coflow," *Proceedings of the Combustion Institute* **29**, 2002, pp. 1881-1888.
3. Utsav, K. C., Silver, J. A., Hovde, D. C., and Varghese, P. L., "Improved multiple-pass Raman spectrometer," *Applied Optics* **50**, 2011, pp. 4805-16
4. Clemens, N. T., "Flow Imaging," *Encyclopedia of Imaging Science and Technology*, 2002, pp. 390-419.
5. Clemens, N. T., and Mungal, M. G., "Two- and Three-Dimensional Effects in the Supersonic Mixing Layer," *AIAA J.* **30**, 1992, pp. 973-981.
6. Thurow, B., Samimy, M., and Lempert, W. R., "Compressibility effects on turbulence structures of axisymmetric mixing layers," *Physics of Fluids* **15**, 2003, p. 1755
7. Elliott, G. S., and Samimy, M., "Compressibility effects in free shear layers," *Physics of Fluids A: Fluid Dynamics* **2**, 1990, p. 1231
8. Goebel, S. G., and Dutton, J. C., "Experimental Study of Compressible Turbulent Mixing Layers," *AIAA J.* **29**, 1991, pp. 538-546.
9. Clemens, N. T., Paul, P. H., Mungal, M. G., and Hanson, R. K., "Scalar Mixing in the Supersonic Shear Layer," Paper 1991-1720, *AIAA 22nd Fluid Dynamics, Plasma Dynamics & Lasers Conference*, Honolulu, HI, 1991.
10. Clemens, N. T., and Paul, P. H., "Scalar measurements in compressible axisymmetric mixing layers," *Physics of Fluids* **7**, 1995, pp. 1071-1081.
11. Dimotakis, P. E., "Two-dimensional shear-layer entrainment," *AIAA J.* **24**, 1986, pp. 1791-1796.
12. Reising, H. H., Kc, U., Voelkel, S. J., Clemens, N. T., Raman, V., Varghese, P. L., and Koo, H., "Vibrational Non-equilibrium Effects in Supersonic Jet Mixing," Paper 2014-0231, *52nd Aerospace Sciences Meeting*, AIAA SciTech, National Harbor, MD, 2014.
13. Cutler, A. D., Cantu, L. M. L., Gallo, E. C. A., Baurle, R., Danehy, P. M., Rockwell, R., Goyne, C., and McDaniel, J., "Nonequilibrium Supersonic Freestream Studied Using Coherent Anti-Stokes Raman Spectroscopy," *AIAA J.* **53**, 2015, pp. 2762-2770.
14. Reising, H. H., Haller, T. W., Clemens, N. T., Varghese, P. L., Fievet, R., and Raman, V., "Spontaneous Raman Scattering Temperature Measurements and Large Eddy Simulations of Vibrational Non-equilibrium in High-Speed Jet Flames," Paper 2016-3550, *32nd AIAA Aerodynamic Measurement Technology & Ground Testing Conference*, Washington, DC, 2016.
15. Voelkel, S., Varghese, P., and Raman, V., "Quasi-State-Specific QCT Method for Calculating the Dissociation Rate of Nitrogen in Thermal Non-Equilibrium," Paper 2016-0449, *54th Aerospace Sciences Meeting*, AIAA SciTech, San Diego, CA, 2016.
16. Y. Paukku, K. R. Yang, Z. Varga, D. G. Truhlar, "Global ab initio ground-state potential energy surface of N<sub>4</sub>," *J. Chemical Physics* **139** (4) 044309, 2013.
17. J. D. Bender, I. Nompelis, P. Valentini, S. Doraiswamy, T. E. Schwartzentruber, G. V. Candler, Y. Paukku, K. R. Yang, Z. Varga, D. G. Truhlar, "Quasiclassical Trajectory Analysis of the N<sub>2</sub>+N<sub>2</sub> Reaction Using a New Ab Initio Potential Energy Surface," Paper

- AIAA-2014-2964, 11th AIAA/ASME Joint Thermophysics and Heat Transfer Conference, AIAA Aviation, Atlanta, GA, 2014.
18. Q. Wang, P. Moin, G. Iaccarino, “A High Order Multivariate Approximation Scheme for Scattered Data Sets,” *J. Computational Physics* **229** (18) 6343-6361, 2010.
  19. Voelkel, S., “Thermal Nonequilibrium Models for High-Temperature Reactive Processes, *Ph.D. dissertation*, The University of Texas at Austin, 2016.
  20. Park, C. “Review of chemical-kinetic problems of future NASA missions. I - Earth entries,” *J. Thermophysics and Heat Transfer* **7**, 1993, pp. 385-398.
  21. Voelkel, S., Raman, V., and Varghese, P. L., “Effect of thermal nonequilibrium on reactions in hydrogen combustion,” *Shock Waves* **26**, 2016, pp. 539-549.
  22. Knab, O., Fruehauf, H.H., Jonas, S., “Multiple temperature descriptions of reaction rate constants with regard to consistent chemical vibrational coupling,” Paper 92-2947, AIAA 27th Thermophysics Conference, (1992)
  23. Knab, O., Fruehauf, H.H., Messerschmid, E.W., “Theory and validation of the physically consistent coupled vibration-chemistry-vibration model,” *J. Thermophys. Heat Transf.* **9**, 1995, pp. 219–226.
  24. Arsentiev, I., Loukhovitski, B., and Starik, A., “Application of state-to-state approach in estimation of thermally nonequilibrium reaction rate constants in mode approximation,” *Chemical Physics* **398**, 2012, pp. 73–80.
  25. Melius, C. F. and Blint, R. J., “The potential energy surface of the HO<sub>2</sub> molecular system,” *Chemical Physics Letters* **64**, 1979, pp. 183–189.
  26. Duchovic, R. J., Volobuev, Y. L., Lynch, G. C., Jasper, A. W., Truhlar, D. G., Allison, T. C., Wagner, A. F., Garrett, B. C., Espinosa-García, J., and Corchado, J. C., POTLIB, <http://comp.chem.umn.edu/potlib>
  27. Koo, H., Raman, V. “Large-Eddy Simulation of a Supersonic Inlet-Isolator,” *AIAA J.* **50**, 2012, pp. 1596–1613.
  28. Koo, H. “*Large-Eddy Simulations of Scramjet Engines*”, *Ph.D. dissertation*, The University of Texas at Austin, 2011.
  29. Koo, H., Donde, P., Raman, V. “A quadrature-based LES/transported probability density function approach for modeling supersonic combustion,” *Proceedings of the Combustion Institute* **33**, 2011, pp. 2203–2210.
  30. Koo, H., Donde, P., Raman, V. “LES-based Eulerian PDF approach for the simulation of scramjet combustors,” *Proceedings of the Combustion Institute* **34**, 2013, pp. 2093–2100.
  31. Donde, P., Koo, H., Raman, V., “A multivariate quadrature based moment method for LES based modeling of supersonic combustion,” *J. Computational Physics* **231**, 2012, pp. 5805–5821.
  32. Fiévet, R. Koo, H., Raman, V. “Numerical simulation of a scramjet isolator with thermodynamic nonequilibrium,” Paper AIAA 2015-3418, 22nd AIAA Computational Fluid Dynamics Conference, AIAA Aviation, Dallas, TX, June 2015.
  33. Millikan, R. C., and White, D. R., “Systematics of Vibrational Relaxation,” *J. Chemical Physics* **39**, 1963, pp. 3209–3213.
  34. Mueller, M. A., Kim, T. J., Yetter, R. A., and Dryer, F. L., “Flow reactor studies and kinetic modeling of the H<sub>2</sub>/O<sub>2</sub> reaction,” *International J. Chemical Kinetics* **31**, 1999, pp. 113–125.

35. Fiévet, R., Voelkel, S., Koo, H., Raman, V., and Varghese, P.L., “Effect of thermal nonequilibrium on ignition in scramjet combustors,” *Proceedings of the Combustion Institute* (2016), <http://dx.doi.org/10.1016/j.proci.2016.08.066>.
36. Fiévet, R., Koo, H., Raman, V., and Auslender, A., “Numerical simulation of shock trains in a 3D channel,” Paper 2016-1018, *54th Aerospace Sciences Meeting*, AIAA SciTech, San Diego, CA, 2016.

## 7. Publications acknowledging this grant

1. Reising, H. H., Kc, U., Voelkel, S., Clemens, N. T., Raman, V., Varghese, P. L. "Vibrational Non-equilibrium Effects in Supersonic Jet Mixing," AIAA Paper 2014-0231, 52<sup>nd</sup> AIAA Aerospace Sciences Meeting, AIAA SciTech, National Harbor, MD, January 2014.
2. Koo, H., Raman, V., Varghese, P., "Direct Numerical Simulation of Supersonic Combustion with Thermal Nonequilibrium," *Proceedings of the Combustion Institute* **35** (2), 2145-2153, 2015.
3. Reising, R., Haller, T., Clemens, N., Varghese, P. "Measurements of Vibrational Non-equilibrium in Supersonic Jet Mixing and Combustion," 67th Annual Meeting of the APS Division of Fluid Dynamics, San Francisco, CA, November 2014.
4. Reising, R., Haller, T., Clemens, N., Varghese, P. "Vibrational Non-equilibrium in Supersonic Jet Mixing and Combustion," Invited, AIAA SciTech 2015, Kissimmee, FL, January 2015.
5. Fiévet, R. Koo, H., Raman, V. "Numerical simulation of a scramjet isolator with thermodynamic nonequilibrium," Paper AIAA 2015-3418, 22nd AIAA Computational Fluid Dynamics Conference, AIAA Aviation, Dallas, TX, June 2015.
6. Voelkel, S. J., Raman, V., Varghese, P. "Vibrational State-Specific Reaction Rates in Hydrogen Combustion," 25th International Colloquium on the Dynamics of Explosions and Reactive Systems (ICDERS), Leeds, UK, August 2015.
7. Fiévet, R., Koo, H., Raman, V., and Auslender, A. "Numerical simulation of shock trains in a 3D channel," Paper 2016-1018, *54th Aerospace Sciences Meeting*, AIAA SciTech, San Diego, CA, 2016.
8. Voelkel, S., Varghese, P., and Raman, V. "Quasi-State-Specific QCT Method for Calculating the Dissociation Rate of Nitrogen in Thermal Non-Equilibrium," Paper 2016-0449, *54th Aerospace Sciences Meeting*, AIAA SciTech, San Diego, CA, 2016.
9. Reising, H. H., Haller, T. W., Clemens, N. T., Varghese, P. L., Fievet, R., Raman, V. "Spontaneous Raman Scattering Temperature Measurements and Large Eddy Simulations of Vibrational Non-equilibrium in High-Speed Jet Flames," Paper 2016-3550, *32nd AIAA Aerodynamic Measurement Technology & Ground Testing Conference*, Washington, DC, 2016.
10. Voelkel, S., Raman, V., Varghese, P. L. "Effect of thermal nonequilibrium on reactions in hydrogen combustion," *Shock Waves* **26**, 2016, pp. 539-549.
11. Fiévet, R., Voelkel, S., Koo, H., Raman, V., Varghese, P.L. "Effect of thermal nonequilibrium on ignition in scramjet combustors," *Proceedings of the Combustion Institute* (2016), <http://dx.doi.org/10.1016/j.proci.2016.08.066>.
12. Voelkel, S., Masselot, D., Varghese, P.L., Raman, V. "Analysis of hydrogen-air detonation waves with vibrational nonequilibrium," *AIP Conference Proceedings* **1786**, 070015 (2016); doi: 10.1063/1.4967591.
13. Fiévet, R., Voelkel, S., Raman, V., Varghese, P. "Numerical investigation of vibrational relaxation coupling with turbulent mixing," Paper 2017-0663, *55th Aerospace Sciences Meeting*, AIAA SciTech, Grapevine, TX, 2017.